SUPERCONDUCTING MAGNETS FOR PARTICLE ACCELERATORS AND STORAGE RINGS

TYPES OF PARTICLE ACCELERATOR

Accelerator Systems

One of the main activities in nuclear and high-energy physics is the study of internal structures of charged particles. The research is carried out by smashing particles into pieces and then analyzing the nature and characteristics of the pieces. The particles are broken by accelerating them to high moments and either blasting them against a fixed target or colliding them among themselves. To increase the event rate, the particles are bunched into a high-intensity beam. The more elementary the particles, the higher the energy needed to smash them. Experiments at the proton scale require beam energies of the order of 1 TeV or more.

The beams of charged particles are produced by accelerator systems made up of several stages, which progressively raise the energy. In the largest machines, the last stage of the accelerator chain, usually referred to as *main ring,* can have a circumference of several tens of kilometers and is installed in an underground tunnel. Such a ring is operated in three phases: (1) *injection,* during which the beam, which has been prepared in various preaccelerators, is injected at low energy, (2) *acceleration,* during which the beam is accelerated to nominal energy, and (3) *storage,* during which the beam is circulated at nominal energy for as long as possible (typically up to 24 h) and is made available for physics experiments. As mentioned above, there are two types of experiments: (1) *fixed-target* experiments, for which the beam is extracted from the main ring to be blasted against a fixed target, and (2) *colliding-beam* experiments, for which two counterrotating beams are blasted at each other. The breakage products are analyzed in large detector arrays surrounding the targets or collision points.

A main ring of a large accelerator system is designed as a synchrotron-type accelerator, and the beam is circulated on an ideally circular orbit, which remains the same throughout injection, acceleration, and storage (1). The charged particles are accelerated by means of electrical fields and are guided and focused by means of magnetic fields. The electrical fields are provided by RF cavities. In large machines, the bending and focusing functions are separated; the former is provided by dipole magnets, whereas the latter is provided by pairs of focusing/defocusing quadrupole magnets (see the discussion that follows). The magnets are arranged around the ring in a regular lattice of cells, which are made up of a focusing quadrupole, a set of bending dipoles, a defocusing quadrupole, and another set of bending dipoles. During acceleration, the field and field gradient of the magnets are raised in proportion to particle momentum to maintain the beam on the design orbit and to preserve its size and intensity.

Bending and Focusing Magnets

Coordinate System Definitions. Let $(O, \boldsymbol{u}, \boldsymbol{v}, \boldsymbol{w})$ designate a rectangular coordinate system, and let (C) be a circle of center O, located in the $(\boldsymbol{u}, \boldsymbol{v})$ plane and representing the design orbit of an accelerator ring. Furthermore, let P be a given point of (C), and let $(P, \boldsymbol{x}, \boldsymbol{y}, \boldsymbol{z})$ designate a rectangular coordinate system associated with P, such that $\boldsymbol{x}$ is a unit vector parallel to (OP), $\boldsymbol{y}$ and $\boldsymbol{w}$ are one and the same, and $\boldsymbol{z}$ is tangent to (C) at P. The x axis defines the horizontal direction, the y axis defines the vertical direction and the z axis corresponds to the main direction of particle motion.

Normal Dipole Magnet. A normal dipole magnet is a magnet, which, when positioned at P, produces within its aperture a magnetic flux density parallel to the $(\boldsymbol{x}, \boldsymbol{y})$ plane and such that

$$B_x = 0 \quad \text{and} \quad B_y = B_1 \tag{1}$$

where B_x and B_y are the x and y components of the flux density and B_1 is a constant.

According to Lorentz' law, a charged particle traveling along the direction of the z axis through the aperture of such a magnet is deflected on a circular trajectory parallel to the horizontal ($\boldsymbol{x}$, $\boldsymbol{z}$) plane. The trajectory radius of curvature χ can be estimated from

$$\chi \approx \frac{E}{0.3\,q\,B_1} \tag{2}$$

Here, χ is in meters, B_1 is in teslas, q is the particle charge in units of electron charge, and E is the particle energy in gigaelectron-volts (GeV). The effect of a dipole magnet on a beam of charged particles is similar in some respects to that of a prism on a light ray.

Equation (2) shows that, to maintain a constant radius of curvature as the particle is accelerated, the dipole field must be ramped up in proportion to particle energy.

Normal Quadrupole Magnet. A normal quadrupole magnet is a magnet, which, when positioned at P, produces within its aperture a magnetic flux density parallel to the (x, y) plane and such that

$$B_x = gy \quad \text{and} \quad B_y = gx \tag{3}$$

where g is a constant referred to as the *quadrupole field gradient* (in teslas per meter).

According to Lorentz' law, a beam of positively charged particles traveling along the direction of the z axis through the aperture of such a magnet is horizontally focused and vertically defocused when g is positive, and vertically focused and horizontally defocused when g is negative. In reference to its action along the x axis on a beam of positively charged particles traveling in the z direction, a magnet with a positive gradient is called a *focusing* quadrupole, while a magnet with a negative gradient is called a *defocusing* quadrupole. To obtain a net focusing effect along both x and y axes, focusing and defocusing quadrupoles must be alternated in the magnet lattice. For either type of quadrupole magnets, the focal length f can be estimated from

$$f \approx \frac{E}{0.3qgl_q} \tag{4}$$

Here, f is in meters, E is in GeV, q is in units of electron charge, g is in teslas per meter, and l_q is the quadrupole magnetic length in meters. The effect of focusing/defocusing quadrupoles on a beam of charged particles is similar to that of convex/concave lenses on a light ray.

Equation (4) shows that to maintain f constant as the particle beam is accelerated, the quadrupole field gradient must be ramped up in proportion to beam energy.

PARTICLE ACCELERATORS AND SUPERCONDUCTIVITY

Why Superconductivity?

Throughout the years, the quest for elementary particles has promoted the development of accelerator systems producing beams of increasingly higher energies. Equation (2) shows that, for a synchrotron, the particle energy is directly related to the product χB_1. Hence, to reach higher energies, we must increase either the accelerator radius or the dipole field (or both). Increasing the accelerator radius means a bigger tunnel. Increasing the dipole field above 2 T implies the use of superconducting magnets. The trade-off between tunneling costs, magnet development costs, and accelerator operating costs is, since the late 1970s, in favor of using superconducting magnets generating the highest possible field and field gradient (2).

Superconductivity is a unique property exhibited by some materials at low temperatures where the resistivity drops to zero. As a result, materials in the superconducting state can transport current without power dissipation by the Joule effect. This offers at least two advantages for large magnet systems such as those needed in accelerator main rings: (1) significant reduction in electrical power consumption and (2) the possibility of relying on much higher overall current densities in the magnets coils. There are, however, at least three drawbacks in using superconducting magnets: (1) the superconductor generates magnetization effects that result in field distortions that have to be corrected (see section on field quality), (2) the magnets must be cooled down and maintained at low temperatures, which requires large cryogenic systems (see section on magnet cooling), and (3) it may happen that an energized magnet, initially in the superconducting state, abruptly and irreversibly switches back to the normal resistive state in a phenomenon referred to as a *quench* (see section on quench performance).

The occurrence of a quench causes an instantaneous beam loss and requires that all or part of the magnet ring be rapidly ramped down to limit conductor heating and possible damage in the quenching magnet (see section on quench protection). Once the quenching magnet is discharged, it can be cooled down again and restored into the superconducting state, and the machine operations can resume. A quench is seldom fatal but is always a serious disturbance. All must be done to prevent it from happening, and all cautions must be taken to ensure the safety of the installation when it does happen.

Review of Superconducting Particle Accelerators

Tevatron. The first large-scale application of superconductivity was the Tevatron, a proton synchrotron with a circumference of 6.3 km built at Fermi National Accelerator Laboratory (FNAL) near Chicago, IL, and commissioned in 1983 (3). The Tevatron now operates as a proton/antiproton collider with a maximum energy of 900 GeV per beam. It relies on about 1000 superconducting dipole and quadrupole magnets, with a maximum operating dipole field of 4 T (4).

HERA. The next large particle accelerator to rely massively on superconducting magnet technology was HERA (Hadron Elektron Ring Anlage) built at DESY (Deutsches Elektronen-SYnchrotron) near Hamburg, Germany, and commissioned in 1990 (5). HERA is an electron/proton collider with a circumference of 6.3 km. It includes two large rings: (1) an electron ring, relying on conventional magnets (maximum energy: 30 GeV), and (2) a proton ring, relying on superconducting magnets (maximum energy: 820 GeV). The maximum operating field of the superconducting dipole magnets is 4.7 T (6).

UNK. Since the early 1980s, the Institute for High Energy Physics (IHEP) located in Protvino, near Moscow, Russia, has

Table 1. Selected Parameters of Major Superconducting Particle Accelerators

Laboratory	FNAL	DESY	IHEP	SSCL	BNL	CERN
Name	Tevatron	HERA	UNK	SSC	RHIC	LHC
Circumference (km)	6.3	6.3	21	87	3.8	27
Particle type	$p\bar{p}$	ep	pp	pp	heavy ions	pp
Energy/beam (TeV)	0.9	0.82	3	20	up to 0.1[a]	7
Number of dipoles	774	416	2168	7944	264	1232[b]
Aperture (mm)	76.2	75	70	50	80	56
Magnetic length (m)	6.1	8.8	5.8	15	9.7	14.2
Field (T)	4	4.68	5.0	6.79	3.4	8.36
Number of quadrupoles	216	256	322	1696	276	386[b]
Aperture (mm)	88.9	75	70	50	80	56
Magnetic length[c] (m)	1.7	1.9	3.0	5.7	1.1	3.1
Gradient (T/m)	76	91.2	97	194	71	223
Commissioning	1983	1990	undecided	cancelled	1999	2005

[a] Per unit of atomic mass.
[b] Two-in-one magnets.
[c] Quadrupoles come in several lengths.

been working on a proton accelerator project named UNK (Uskoritelno-Nakopitelniy Komplex). The circumference of the UNK main ring is 21 km for a maximum energy of 3 TeV in a fixed target mode (7). The maximum operating dipole field is 5 T (8). A number of superconducting dipole and quadrupole magnet prototypes have been built and cold-tested, and the tunnel is almost completed, but, given the present (1998) economic situation in Russia, the future of the machine is undecided.

SSC. In the mid 1980s, the United States started the Superconducting Super Collider (SSC) project, a giant proton–proton collider with a maximum energy of 20 TeV per beam (9). The last stage of the SSC complex would have been made up of two identical rings of superconducting magnets installed on top of each other in a tunnel with a circumference of 87 km. The maximum operating dipole field was 6.8 T. The project was eventually canceled in October 1993 by decision of the US Congress, after 12 miles of tunnel had been dug near Dallas, TX, and a successful superconducting magnet R&D program had been carried out (10).

RHIC. Brookhaven National Laboratory (BNL), located on Long Island, NY, will complete the construction in 1999 on its site of the Relativistic Heavy Ion Collider (RHIC). RHIC is designed to collide beams of nuclei as heavy as gold, accelerated in two identical rings to energies between 7 and 100 GeV per beam and per unit of atomic mass (11). Each ring has a circumference of 3.8 km; the maximum operating dipole field is 3.4 T (12).

LHC. In December 1994, the European Laboratory for Particle Physics (CERN) approved the construction of the Large Hadron Collider (LHC) in its existing 27-km-circumference tunnel located at the Swiss/French border, near Geneva, Switzerland (13). LHC will be a proton/proton collider with a maximum energy of 7 TeV per beam. It will have a single ring of so-called *twin-aperture* superconducting magnets, housing within the same mechanical structure, the pipes for two counterrotating proton beams (14). The maximum operating dipole field is set at 8.36 T. Commissioning is planned for 2005.

Prominent Features of Superconducting Accelerator Magnets

Selected parameters of the major projects of superconducting particle accelerators are summarized in Table 1, whereas Fig. 1(a–e) presents cross-sectional views of the Tevatron, HERA, SSC, RHIC, and LHC dipole magnets (15).

The magnets rely on similar design principles, which are detailed in the following sections. The field is produced by saddle-shaped coils that, in their long straight sections, approximate cos $n\theta$ distributions of conductors (with $n = 1$ for dipole magnets and $n = 2$ for quadrupole magnets). The coils are wound from Rutherford-type cables made of NbTi multifilamentary strands and are mechanically restrained by means of laminated collars. The collared-coil assembly is placed within an iron yoke providing a return path for the

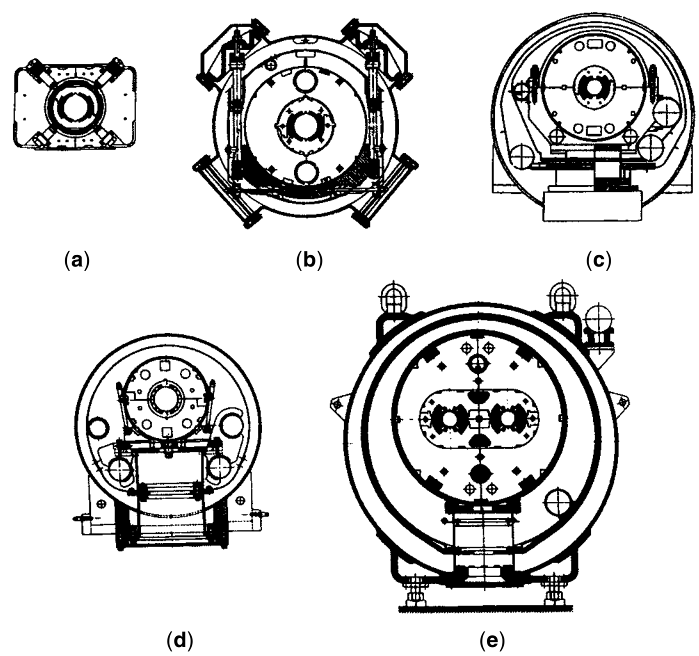

Figure 1. Cross-sectional views of superconducting dipole magnets for large particle accelerators (15): (a) Tevatron, (b) HERA, (c) SSC, (d), RHIC, and (e) LHC.

magnetic flux. In the case of the Tevatron, the collared-coil assembly is cold, whereas the iron yoke is warm. Starting with HERA, the iron yoke is included in the magnet cryostat, and the cold mass is completed by an outer shell delimiting the region of helium circulation. The cold mass of the LHC magnets includes two collared-coil assemblies within a common yoke. Tevatron, HERA, UNK, SSC, and RHIC magnets are cooled by boiling helium at 1 atm (4.2 K) or supercritical helium at 3 atm to 5 atm (between 4.5 K and 5 K), whereas LHC magnets are cooled by superfluid helium at 1.9 K (1 atm $\approx$ 0.1 MPa).

Superconducting Accelerator Magnet R&D

A number of laboratories are presently involved in R&D work on high field or high field gradient accelerator magnets. Among them is Twente University, located near Enschede in the Netherlands, which, in 1995, cold-tested at CERN a short model dipole magnet (made with Nb_3Sn cable), which reached 11 T on its first quench at 4.4 K (16). Soon after, in early 1997, Lawrence Berkeley National Laboratory (LBNL), located in Berkeley, CA, cold-tested a short dipole magnet model (also made with Nb_3Sn cable), which, after a number of training quenches, reached a record dipole field of 13.5 T at 1.8 K (17).

CONDUCTOR AND CONDUCTOR INSULATION

Superconducting Material

The most widely used superconducting material is a metallic alloy of niobium and titanium (NbTi), with a Ti content between 45% and 50% in weight (18). NbTi is easy to mass-produce and has good mechanical properties. It is a type-II superconductor, with a coherence length ξ of 5 nm, and a London penetration depth λ, of 300 nm (chapter 2 of Ref. 2).

The upper critical magnetic flux density of NbTi, B_{C2}, can be estimated as a function of temperature T using

$$B_{C2}(T) = B_{C20}\left[1 - \left(\frac{T}{T_{C0}}\right)^{1.7}\right] \tag{5}$$

where B_{C20} is the upper critical magnetic flux density at zero temperature (about 14.5 T) and T_{C0} is the critical temperature at zero field (about 9.2 K).

The critical current density of NbTi, J_C, can be parametrized as a function of temperature, magnetic flux density, B, and critical current density at 4.2 K and 5 T, J_{Cref}, using (19):

$$\frac{J_C(B,T)}{J_{Cref}} = \frac{C_0}{B}\left[\frac{B}{B_{C2}(T)}\right]^{\alpha}\left[1 - \frac{B}{B_{C2}(T)}\right]^{\beta}\left[1 - \left(\frac{T}{T_{C0}}\right)^{1.7}\right]^{\gamma} \tag{6}$$

where C_0, α, β, and γ are fitting parameters. (Typical values for LHC strands are C_0 = 30 T, α = 0.6, β = 1.0, and γ = 2.0.) Since the time of the Tevatron, a factor of about 2 has been gained on the critical current density at 4.2 K and 5 T, and values in excess of 3000 A/mm^2 are now obtained in industrial production (20).

The highest dipole field reached on a NbTi magnet is 10.53 T at 1.77 K (21). Magnet designers consider that this is about the limit for NbTi and that to produce higher fields, it is necessary to change the material. The only other material that is readily available at (small) industrial scale is an intermetallic compound of niobium and tin (Nb_3Sn) belonging to the A15 crystallographic family (18). Nb_3Sn presents interesting superconducting properties (e.g., its upper critical field at zero temperature and zero strain is in excess of 25 T) (22). However, its formation requires a heat treatment at temperatures up to 700°C for times up to 300 h. Furthermore, once it is reacted, it becomes very brittle, and its superconducting properties are strain-sensitive. Hence, Nb_3Sn calls for special fabrication techniques, which, so far, have limited its use. In recent years, significant R&D work has been carried out to improve the performance of Nb_3Sn wires, thanks to the International Thermonuclear Experimental Reactor (ITER) program (23,24).

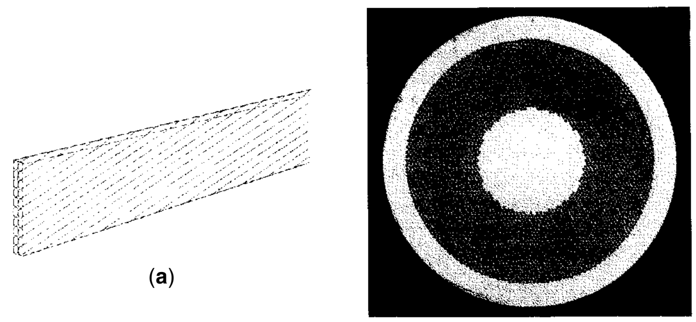

(b)

Figure 2. Rutherford-type cable for accelerator magnet: (a) cable sketch and (b) cross-sectional view of a cable strand.

Although great progress has been made in the development of so-called *high-temperature superconductor* (HTS), such as bismuth copper oxides, $Bi_2Sr_2CaCu_2O_x$ and $(Bi,Pb)_2Sr_2Ca_2Cu_3O_x$, and yttrium copper oxides, $YBa_2Cu_3O_7$, these materials are not ready yet for applications requiring low-cost, mass-production, and high-critical current density (25).

Rutherford-Type Cable

Superconducting accelerator magnet coils are wound from so-called *Rutherford-type* cables. As illustrated in Fig. 2(a), a Rutherford-type cable consists of a few tens of strands, twisted together, and shaped into a flat, two-layer, slightly keystoned cable (26). The strands themselves consist of thousands of superconducting filaments, twisted together and embedded in a matrix of normal metal (18). Except for the cables used in a few R&D model magnets, the filaments are made of NbTi, and the matrix is high-purity copper. The strand diameter ranges from 0.5 mm to 1.3 mm, and the filament diameter ranges from 5 μm to 15 μm. Figure 2(b) presents a cross-sectional view of a typical SSC strand.

The small radii of curvature of the coil ends preclude the use of a monolithic conductor because it would be too hard to bend. A multistrand cable is preferred to a single wire for at least four reasons: (1) it limits the piece length requirement for wire manufacturing (a coil wound with a N-strand cable requires piece lengths which are $1/N$ shorter than for a similar coil wound with a single wire), (2) it allows strand-to-strand current redistribution in the case of a localized defect or when a quench originates in one strand (27,28), (3) it limits the number of turns and facilitates coil winding, and (4) it limits coil inductance (the inductance of a coil wound with a N-strand cable is $1/N^2$ smaller than that of a similar coil wound with a single wire). A smaller inductance reduces the voltage requirement on the power supply to ramp-up the magnets to their operating current in a given time and limits the maximum voltage to ground in case of a quench (see quench protection section). The main disadvantage of using a cable is the high operating current (over a few thousand amperes), which requires large current supplies and large current leads.

The main issues for strand design and manufacturing are (1) copper-to-superconductor ratio, which should not be too small to limit conductor heating in case of a quench while achieving a high overall critical current; (2) filament size, to limit field distortions resulting from superconductor magnetization at low field (see section on field quality); (3) superconductor critical current density, which can be improved by improving pinning and filament uniformity (18) and (4) piece length.

The main issues for cable design and fabrication are (1) compaction, which should be large enough to ensure good mechanical stability and high overall current density while leaving enough void (typically a few percent in volume) for liquid helium cooling; (2) control of outer dimensions to achieve suitable coil geometry and mechanical properties; (3) limitation of critical current degradation due to strand and filament deformations at the cable edges (29,30), and (4) control of interstrand resistance, which should not be too small to limit field distortions induced by coupling currents while ramping (see section on field quality) and should not be too large to allow current redistribution among cable strands.

The interstrand resistance can be modified by oxidizing or by coating the strand surface (31,32). Also, a thin, insulating foil (such as stainless steel) can be inserted between the two-strand layers of the cable (33). The strands used in HERA and LHC cables are coated with a silver-tin solder, called *stabrite*. Half of the strands of the Tevatron cable are coated with stabrite, whereas the other half are insulated with a black copper oxide, called *ebanol*. UNK, SSC, and RHIC cables rely on natural oxidation. Up to now, no foiled cable has been used in a magnet.

Note that at the end of cabling, the high purity copper of the strand matrix is heavily cold-worked and that it may require an annealing procedure.

Cable Insulation

The main requirements for cable insulation are (1) good dielectric strength in a helium environment and under high transverse pressure (up to 100 MPa), (2) small thickness (to maximize overall current density in the magnet coil) and good physical uniformity (to ensure proper conductor positioning for field quality), (3) retention of mechanical properties over a wide temperature range (from helium temperature to coil curing temperature—see the discussion that follows), and (4) ability to withstand radiation in an accelerator environment. In addition, the insulation system is required to provide a means of bonding the coil turns together to give the coil a semirigid shape and facilitate its manipulation during the subsequent steps of magnet assembly. It is also desirable that the insulation be somewhat porous to helium for conductor cooling. Note that the dielectric strength of helium gas at 4.2 K is far worse than that of liquid helium and that it degrades significantly with increasing temperature (34).

The insulation of Tevatron, HERA, and UNK magnets, of most SSC magnets, and of the early LHC models is made up of one or two inner layers of polyimide film, wrapped helically with a 50% to 60% overlap, completed by an outer layer of resin-impregnated glass tape, wrapped helically with a small gap. The inner layer is wrapped with an overlap for at least two reasons: (1) the polyimide film may contain pinholes that must be covered (the probability of having two superimposed pin holes in the overlapping layer is very low) and (2) the Tevatron experience has shown that it was preferable to prevent the resin impregnating the glass wrap from entering in contact with the NbTi cable (the energy released by cracks in the resin is believed to be sufficient to initiate a quench) (Ref. 4, p. 784). The outer layer is wrapped with a gap to set up helium cooling channels between coil turns. The resin is of a thermosetting type and requires heat to increase cross-link density and cure into a rigid bonding agent. The curing is realized after winding completion in a mold of very accurate dimensions to control coil geometry and Young's modulus (35).

RHIC magnets and the most recent LHC models use a so-called *all-polyimide* insulation where the outer glass wrap is replaced by another layer of polyimide film with a polyimide adhesive on its surface (36). The all-polyimide insulation has a better resistance to puncture, but the softening temperature of the adhesive can be higher than the temperature needed to cure a conventional resin (225°C for RHIC-type all-polyimide insulation compared to 135°C for SSC-type polyimide/glass insulation).

MAGNETIC DESIGN

Field Produced by Simple Current-Line Distributions

Single Current-Line in Free Space. Let (O, $\boldsymbol{x}$, $\boldsymbol{y}$, $\boldsymbol{z}$) designate a rectangular coordinate system, and let ($-I$, R, θ) designate a current-line of intensity ($-I$), parallel to the z axis, and located at a position $\boldsymbol{s} = R\exp(i\theta)$ in the complex (O, $\boldsymbol{x}$, $\boldsymbol{y}$) plane, as represented in Fig. 3(a). (The current-line intensity is chosen to be negative to end up with a positive factor in the right member of Eq. (8).) The magnetic flux density $\boldsymbol{B}$, produced by this current-line in free space, can be computed using Biot and Savart's law. It is uniform in z and parallel to the ($\boldsymbol{x}$, $\boldsymbol{y}$)

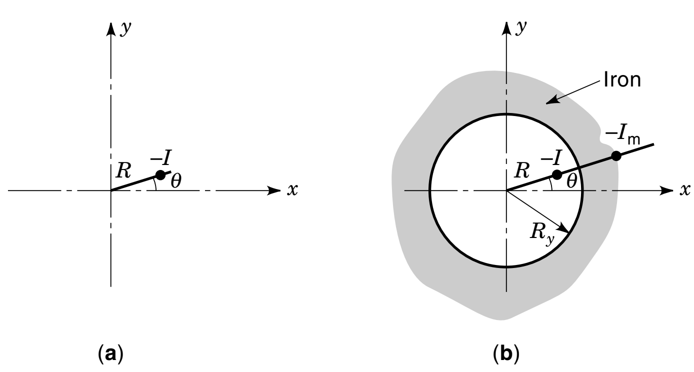

Figure 3. Representations of a single current-line: (a) in a vacuum and (b) inside a circular iron yoke.

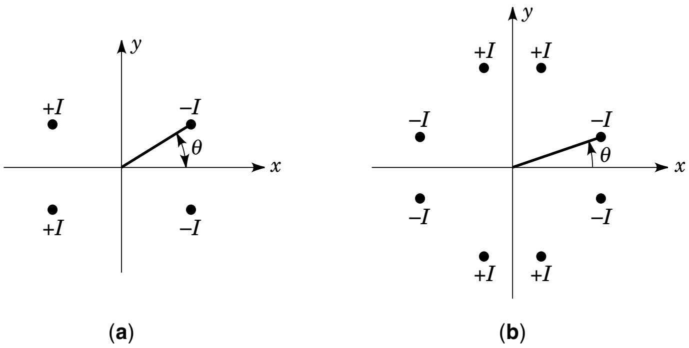

Figure 4. Examples of current-line distributions with selected symmetries (a) quadruplet of current-lines with an even symmetry about the x axis and an odd symmetry about the y axis and (b) octuplet of current-lines with even symmetries with respect to the x and y axes and odd symmetries with respect to the first and second bisectors.

plane. It can be expanded into a power series of the form (37)

$$B_y + iB_x = \sum_{n=1}^{+\infty}(B_n + iA_n)\mathbf{z}^{n-1} \quad \text{for } \mathbf{z} = x + iy,\ |\mathbf{z}| < R \tag{7}$$

where B_x and B_y are the x and y components of $\boldsymbol{B}$, and A_n and B_n are constant coefficients, referred to as *skew* and *normal* $2n$-pole field coefficients, given by

$$B_n + iA_n = \frac{\mu_0 I}{2\pi R^n}[\cos(n\theta - i\sin(n\theta)] \tag{8}$$

Single Current-Line within a Circular Iron Yoke. Let us now assume that the current-line of Fig. 3(a) is located inside a circular iron yoke of inner radius R_y, as represented in Fig. 3(b). The contribution of the iron yoke to the magnetic flux density can be shown to be the same as that of a mirror current-line, of intensity $(-I_{\mathrm{m}})$, and position $\mathbf{s}_{\mathrm{m}}$ in the complex plane, where

$$I_{\mathrm{m}} = \frac{\mu - 1}{\mu + 1} I \quad \text{and} \quad \mathrm{s}_{\mathrm{m}} = \frac{R_y^2}{\mathbf{s}^*} \tag{9}$$

Here μ designates the relative magnetic permeability of the iron yoke, and $\mathbf{s}^*$ designates the complex conjugate of $\mathbf{s}$. Note that the mirror image method is applicable only if the iron yoke is not saturated and as long as its permeability is uniform.

Quadruplet of Current-Lines with Dipole Symmetry. Using these expressions, the magnetic flux densitity produced by the quadruplet of current-lines $(-I, R, \theta)$, $(+I, R, \pi - \theta)$, $(+I, R, \pi + \theta)$ and $(-I, R, -\theta)$, represented in Fig. 4(a), can be estimated from the power series expansion

$$B_y + \mathrm{i}B_x = \sum_{k=0}^{+\infty} B_{2k+1}\mathbf{z}^{2k} \quad \text{for } \mathbf{z} = x + iy,\ |\mathbf{z}| < R \tag{10}$$

where

$$B_{2k+1} = \frac{2\mu_0 I}{\pi R^{2k+1}}\cos[(2k+1)\theta] \tag{11}$$

The first term ($k = 0$) of the series corresponds to a pure normal dipole field parallel to the y axis. The B_{2k+1} coefficients are called the *allowed* multipole field coefficients of this current distribution.

Octuplet of Current-Lines with Quadrupole Symmetry. Similarly, the magnetic flux density produced by the octuplet of current-lines represented in Fig. 4(b) is given by

$$B_y + iB_x = \sum_{k=0}^{+\infty} B_{4k+2}\mathbf{z}^{4k+1} \quad \text{for } \mathbf{z} = x + iy,\ |\mathbf{z}| < R \tag{12}$$

where

$$B_{4k+2} = \frac{4\mu_0 I}{\pi R^{4k+2}}\cos[(4k+2)\theta] \tag{13}$$

The first term ($k = 0$) of the series corresponds to a pure normal quadrupole field whose axes are parallel to the first and second bisectors. For this current distribution, the allowed multipole field coefficients are the normal $(4k + 2)$-pole field coefficients.

Two-Dimensional Geometry

Symmetry Considerations. The field computations presented in the previous section showed that current distributions with the symmetries of Fig. 4(a) (i.e., even with respect to the x axis and odd with respect to the y axis) were suitable for generating dipole fields, whereas current distributions with the symmetries of Fig. 4(b) (i.e., even with respect to the x and y axes and odd with respect to the first and second bisectors) were suitable for generating quadrupole fields. Starting from these premises, the coil geometry can be optimized to obtain the required dipole or quadrupole field strength within the magnet aperture. In addition, in most accelerator designs, it is required that high-order multipole field coefficients be as small as possible. Hence, the coil geometry optimization is also carried out to minimize the contributions from nondipole or nonquadrupole terms.

cos $n\theta$ Coil Designs. The coil geometry most commonly used for a dipole magnet is composed of the cylindrical current shells shown in Fig. 5(a). The magnetic flux density produced by such shells can be computed by dividing them up into quadruplets of current-lines having the symmetry of Fig. 4(a) and by summing their contributions over a shell quadrant. It follows that the magnetic flux density is again given by Eq.

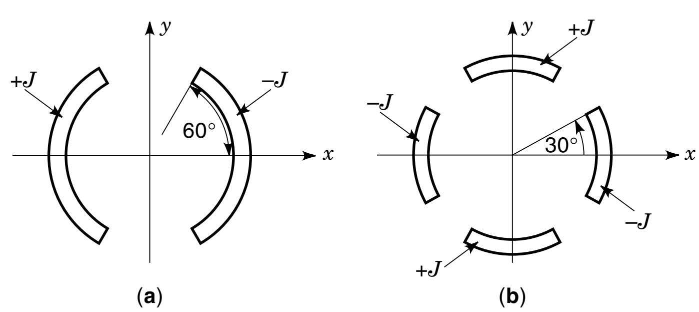

Figure 5. Current shell approximations for the generation of multipole fields: (a) dipole field and (b) quadrupole field.

(10), but the expressions of the multipole field coefficients become

$$B_1 = \frac{2\mu_0 J}{\pi}(R_\mathrm{o} - R_\mathrm{i})\sin\theta_0 \tag{14a}$$

and

$$B_{2k+1} = \frac{2\mu_0 J}{\pi(2k+1)(2k-1)}\left(\frac{1}{R_\mathrm{i}^{2k-1}} - \frac{1}{R_\mathrm{o}^{2k-1}}\right)\sin[(2k+1)\theta_0] \quad \text{for } k, k \geq 1 \tag{14b}$$

Here, R_i and R_o are the inner and outer radii of the shells, θ_0 is the pole angle, and J is the overall current density, which is assumed to be uniform. Note that B_3 (first allowed multipole field coefficient after B_1 in a current distribution with a dipole symmetry) is nil for $\theta_0 = \pi/3$.

Similarly, the coil geometry most commonly used for a quadrupole magnet is made up of the cylindrical current shells shown in Fig. 5(b). The magnetic flux density is here given by Eq. (12), where

$$B_2 = \frac{2\mu_0 J}{\pi}\ln\left(\frac{R_0}{R_\mathrm{i}}\right)\sin 2\theta_0 \tag{15a}$$

and

$$B_{4k+2} = \frac{\mu_0 J}{\pi k(4k+2)}\left(\frac{1}{R_\mathrm{i}^{4k}} - \frac{1}{R_\mathrm{o}^{4k}}\right)\sin[(4k+2)\theta_0] \quad \text{for } k, k \geq 1 \tag{15b}$$

Note that B_2 corresponds to the quadrupole field gradient g and that B_6 (first allowed multipole field coefficient after B_2 in a current distribution with a quadrupole symmetry) is nil for $\theta_0 = \pi/6$.

By reference to the conductor distribution around the circular inner bore, such coil geometries are referred to as cos θ and cos 2θ designs. They are very compact and make the most effective use of conductors by bringing them close to the useful aperture.

Current Shell Approximations. In practice, the current shells of Figs. 5(a) and 5(b) are approximated by stacking into an arch the slightly keystoned cables described in the conductor section. High-field dipole or high-field-gradient quadrupole magnets usually rely on two coil layers whose contributions add up. Also, wedges are introduced between some of the coil turns to separate the conductors into blocks. The blocks angles are then optimized to eliminate high-order multipole field coefficients (37).

In the case of Tevatron, HERA, and UNK magnets, the cable keystone angle is large enough to allow the formation of an arch with the desired aperture. Furthermore, each coil turn lies along a radius vector pointing towards the aperture center. In the case of SSC and LHC magnets, the coil aperture is reduced to minimize the volume of superconductor. This results in a keystone angle requirement deemed unacceptable from the point of view of cabling degradation. Hence, in these magnets, the cables are not sufficiently keystoned to assume an arch shape, and the wedges between conductor blocks must be made asymmetrical to compensate for this lack (38). Also, the coil turns end up being nonradial, as illustrated in Fig. 6, which shows the conductor distribution in a quadrant of a 50-mm-aperture SSC dipole magnet coil (the vectors represent the components of the Lorentz force discussed in the section on mechanical design).

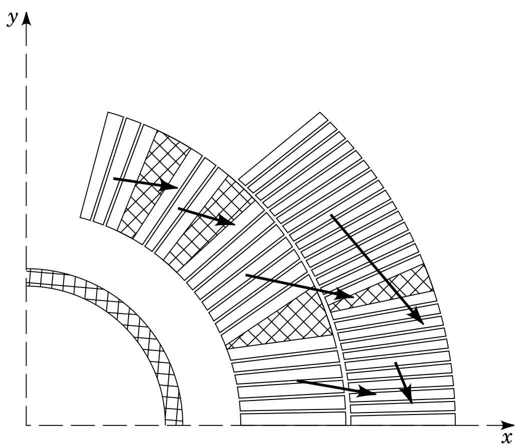

Figure 6. Conductor and Lorentz force distributions in a quadrant of a 50-mm-aperture SSC dipole magnet coil (38).

Note that the magnetic flux density produced by the coil of Fig. (6) can be accurately computed by dividing each turn into two rows of elementary current-lines parallel to the z axis and approximately equal in number to the number of cable strands (Ref. 39, p. 226).

Iron Yoke Contribution. The coils of particle accelerator magnets are usually surrounded by an iron yoke, which provides a return path for the magnetic flux while enhancing the central field or field gradient.

As an illustration, let us place the cylindrical current shells of Fig. 5(a) within a circular iron yoke of inner radius R_y. The contribution of the iron yoke to the normal $(2k + 1)$-pole field coefficient B_{2k+1}^{y} can be estimated as (Ref. 2, p. 53)

$$B_{2k+1}^{\mathrm{y}} = \frac{\mu - 1}{\mu + 1}\left(\frac{R_\mathrm{i} R_\mathrm{o}}{R_y^2}\right)^{2k+1} B_{2k+1}^{\mathrm{s}} \tag{16}$$

where μ is the relative magnetic permeability of the iron yoke, R_i and R_o are the current shell inner and outer radii, and B_{2k+1}^{s} is the $(2k + 1)$-pole field coefficient produced by the current shell alone.

Equation (16) shows that the smaller R_y, the larger the field enhancement. However, there are two limitations on how close the iron can be brought to the coils: (1) room must be left for the support structure, and (2) iron saturates for fields above 2 T, resulting in undesirable distortions (see section on field quality).

As already mentioned, the Tevatron magnets use a warm iron yoke (i.e., placed outside the helium containment and vaccum vessel), but starting with HERA magnets, the iron yoke is included within the magnet cold mass. For SSC dipole magnets, the field enhancement due to the iron yoke is of the order of 20%. In LHC magnets, two coil assemblies (powered with opposite polarity) are placed within a common iron yoke. This twin-aperture design results in left–right asymmetries in the yoke surrounding each coil assembly taken individually. These asymmetries must be taken into account when calculating the field quality.

Operating Margin. Equations 14(a) and 15(a) show that, to achieve high fields and high field gradients, it is desirable to maximize the overall current density in the magnet coil. This can be done by three means: (1) maximizing the superconductor performance, (2) minimizing the copper-to-superconductor ratio in the cable strands, and (3) minimizing the turn-to-turn insulation thickness. As explained in other sections, there are lower bounds on the values of copper-to-superconductor ratio and insulation thickness in order to limit conductor heating in case of quenching and to ensure proper electrical insulation. As for the superconductor, the upper limit is the critical current density at the given temperature and magnetic flux density.

The magnetic flux density to which the conductor is exposed is nonuniform over the magnet coil, but the maximum current-carrying capability of the conductor is determined by the section where the magnetic flux density is the highest. In most cases, this corresponds to the pole turn of the innermost coil layer. Let $B_p = f(I)$ designate the peak magnetic flux density on the coil as a function of supplied current I, and let $I_C = f(B)$ designate the supposedly known cable critical current as a function of applied magnetic flux density B. The intersection between these two curves determines the maximum quench current of the magnet I_{qm}.

In practice, magnets must be operated below I_{qm} so as to ensure that the superconductor is in the superconding state and to limit the risks of quenching. Let I_{op} designate the operating current. Then, the current margin of the magnet m_I is defined as

$$m_I = 1 - \frac{I_{op}}{I_{qm}} \tag{17}$$

The excellent quench performance of the HERA magnets (6) suggests that the current margin can be set to as little as 10%, but it is safer to aim for 20%.

In comparison to other superconducting magnets, such as solenoids for magnetic resonance imaging, a current margin of 10% to 20% is quite small. This implies that accelerator magnets are operated very close to the superconductor critical surface and that they are very sensitive to any kind of disturbances that may cause the magnet to cross the critical surface and lead to a quench.

A peculiarity of a two-layer, cos θ dipole magnet coil design is that the peak field in the outermost layer is quite a bit lower than in the innermost layer. Hence, when using the same cable and current for both layers, the outer layer is operated with a much higher current margin than the inner layer, which can be considered as a waste of costly superconductor. SSC and LHC dipole magnet coils use a smaller conductor for the outer layer than for the inner layer. This results in a higher overall current density in the outer layer and reduces the difference in current margins. Such action is referred to as conductor *grading.* The main disandvatage of grading is that it requires splices between inner and outer layer cables (which, of course, are connected electrically in series and only require one power supply).

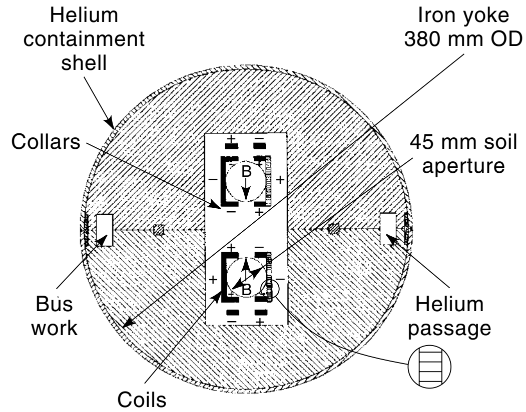

Figure 7. Conceptual block design developed at BNL for a high field, twin-aperture dipole magnet (41).

Limits of cos $n\theta$ Design. The cos $n\theta$ coil design has been very successful until now, with a record dipole field of 13.5 T reached by the LBNL short dipole magnet model (using Nb_3Sn cables at 1.8 K). However, it has two main drawbacks: (1) the coil ends are difficult to make (see the section on coil ends), and (2) due to the Lorentz force distribution, a stress accumulation in the azimuthal direction results in high transverse pressures on the midplane conductors (see Fig. 6). For very high field magnets, requiring the use of A15 (or even possibly HTS) superconductors, which are strain-sensitive, these high transverse pressures can result in significant critical current degradation (40).

Alternative coil designs, which may allow better management of the Lorentz stresses within the magnet coil, are being investigated. As an illustration, Fig. 7 presents a conceptual *block* or *window-frame* design developed at BNL for a twin-aperture dipole magnet relying only on simple, *racetrack* coils (41). Note, however, that such designs make less effective use of superconductor.

Coil End Design

One of the main difficulties of the cos $n\theta$ design is the realization of coil ends. In the coil straight section, the conductors run parallel to the magnet axis, but, in the coil ends, the conductors must be bent sharply with small radii of curvature to make U-turns over the beam tube that is inserted within the magnet aperture. This confers to the coil a *saddle shape* as illustrated in Fig. 8.

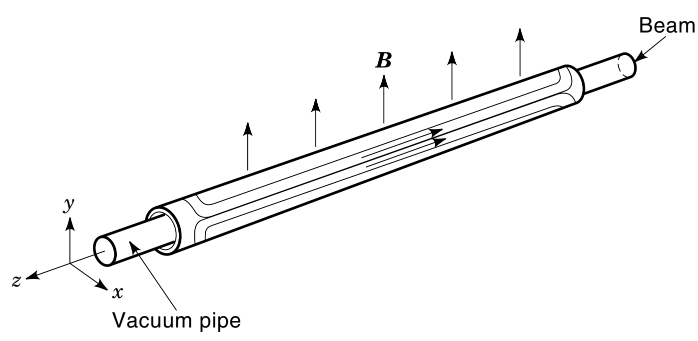

Figure 8. Perspective view of a saddle-shaped coil assembly for a dipole magnet.

Sophisticated algorithms have been developed to determine the conductor trajectories that minimize strain energy (42). These algorithms, which often require winding tests to determine correction factors, are coupled with electromagnetic computations to minimize field distortions. SSC and LHC magnets use precisely machined end spacers, designed by the optimization programs, which are positioned between conductor blocks (43). In addition, the iron yoke does not extend over the coil ends, to reduce the field on the conductors and ensure that the peak field is located in the coil straight section where the conductors can be better supported.

Sagitta

To limit the number of coil ends and of magnet interconnects around the accelerator ring, the arc dipole and quadrupole magnets are made as long as possible. The circulation of a charged beam in a dipole magnet, of magnetic length l_{d}, results in an angular deflection ϕ of the particle trajectory, which can be estimated as

$$\phi \approx \frac{0.3qB_1 l_{\mathrm{d}}}{E} = \frac{l_{\mathrm{d}}}{x} \tag{18}$$

Here, ϕ is in radians and l_{d} is in meters, B_1 is the dipole magnetic flux density in teslas, q is the particle charge in units of electron charge, and E is the particle energy in GeV.

As a result, long dipole magnets must be slightly bent to accompany the particle trajectory. This bending, which is implemented in the ($\boldsymbol{x}$, $\boldsymbol{z}$) plane, is referred to as *sagitta*.

FIELD QUALITY

Multipole Expansion

Except near the short coil ends, the magnetic flux density produced in the bore of a particle accelerator magnet can be considered as two-dimensional. The power series expansion of Eq. (7) is usually rewritten in the more convenient form

$$\begin{gathered} B_y + \mathrm{i}B_x = B_{\mathrm{r}} 10^{-4} \sum_{n=1}^{+\infty} (b_n + \mathrm{i}a_n) \left(\frac{\mathbf{z}}{R_{\mathrm{r}}}\right)^{n-1} \\ \text{for } \mathbf{z} = x + \mathrm{i}y,\ |\mathbf{z}| < R_{\mathrm{i}} \end{gathered} \tag{19}$$

where B_x and B_y are the x and y components of the magnetic flux density, R_{r} is a reference radius representative of the maximum beam size (R_{r} was 10 mm for the SSC and is now 17 mm for the LHC), B_{r} is the absolute value of the dipole or quadrupole component at R_{r}, a_n and b_n are the dimensionless skew and normal $2n$-pole coefficients, and R_{i} is the coil inner radius. Note the presence of the 10^{-4} scale factor.

Given the symmetries of current distributions in magnet coil assemblies, and as explained in the previous section, only selected normal multipole coefficients are expected to be nonzero. These allowed multipole coefficients can be tuned up by iterating on the electromagnetic design. In practice, however, nonuniformities in material properties and manufacturing errors result in symmetry violations that produce unallowed multipole coefficients. For instance, a top/bottom asymmetry in a dipole magnet produces a nonzero skew quadrupole coefficient (a_2), whereas a left/right asymmetry produces a nonzero normal quadrupole coefficient (b_2). These unwanted coefficients can be eliminated only by improving material selection, tooling, and assembly procedures.

Field Quality Requirements

From the accelerator point of view, the beam optics is primarily governed by integrated field effects over the magnet ring. The main field quality requirements are (1) suitable dipole field integral and small dipole field angle variations [the former to ensure that the integrated bending angle over the magnet ring is (2π) and the latter to ensure that the particle trajectory is planar], (2) accurate quadrupole alignment and suitable quadrupole field integral (the former to avoid coupling of particle motions along the x and y axes and the latter to ensure proper focusing), and (3) small high-order multipole coefficients (to ensure large beam dynamic aperture). In the case of high-order multipole coefficients, it is customary to specify tables of mean values and standard deviations over the entire magnet population (44). The tables of mean values are referred to as *systematic* multipole specifications, whereas those of standard deviations are referred to as *random* multipole specifications. The specified values are all expressed at the reference radius R_{r}.

In large machines such as SSC or LHC, the dipole and quadrupole field integrals must be controlled with a relative precision of the order of 10^{-3}. The variations in dipole field angles must be kept within a few milliradians, and the tolerance on quadrupole alignement is of the order of 0.1 mm. Systematic and random multipole specifications are given up to the 18th or 20th pole and get tighter with increasing pole order. For SSC magnets at 10 mm, the specifications went from a few tenths of a unit for low-order coefficients to a few thousandths of a unit for higher-order coefficients.

Geometric Errors

Types of Geometric Errors. The specifications on multipole coefficients require that the individual conductors and the yoke surrounding the coil assembly be positioned with a very good accuracy (typically a few hundredths of a millimeter in the two-dimensional cross section). Improper positioning results in geometric errors that distort the central field and produce unwanted multipole coefficients.

The geometric errors can be classified in at least five categories: (1) errors in coil inner and outer radii and in yoke inner radius; (2) errors in coil pole angle, wedge angle, and conductor angular distribution; (3) symmetry violations in coil assembly; (4) centering errors with respect to the iron yoke; and (5) residual twist of magnet assembly.

Effects of Azimuthal Coil Size Mismatch. A common cause of geometric error is a mismatch between the azimuthal sizes of the various coils constituting a coil assembly. Such mismatch results in displacements of the coil assembly symmetry planes that produce nonzero, low-order unallowed multipole coefficients (45). For instance, a mismatch between the azimuthal sizes of the top and bottom coils used in a dipole magnet coil assembly causes an upward or downward displacement of the coil parting planes, which produces a nonzero skew quadrupole coefficient a_2. Similarly, a systematic mismatch between the left and right sides of the coils used in a dipole magnet coil assembly causes a rotation of the coil parting planes, which produces a nonzero skew sextupole coefficient a_3. A systematic a_2 can be limited by randomly mixing coil production, whereas the occurrence of a systematic a_3 can be avoided only by correcting tooling.

Iron Saturation

When the field in the iron yoke is less than 2 T, the relative magnetic permeability of the yoke can be considered as very large and uniform, and the iron contribution to the central field increases linearly as a function of tranport current in the magnet coil. For fields above 2 T, parts of the iron start to saturate, and their relative magnetic permeability drops. As a result, the iron contribution becomes a less-than-linear function of transport current. This relative decrease in iron contribution appears as a sag in the magnet transfer function (38). (The transfer function is defined as the ratio of B_r to the transport current.) The transfer function sag can exceed a few percent in dipole magnets but is usually negligible in quadrupole magnets.

In the case of a single-aperture magnet with a symmetrical iron yoke, the saturation first occurs in the pole areas producing a positive shift in normal sextupole coefficient b_3. At higher currents, the saturation reaches the midplane areas, producing a negative shift in b_3, which partially compensates for the effects of pole saturation. The midplane saturation can be forced to occur sooner by punching notches (i.e., removing matter) at appropriate locations in the yoke. As an illustration, Fig. 9 presents measurements of b_3 as a function of current in the central part of a SSC dipole magnet prototype. The measurements above 3 kA clearly show the effect of pole saturation at high currents (the origin of the hysteresis is explained in the next section).

In the case of a twin-aperture dipole, the central part of the yoke saturates before the outer parts, resulting in left/right asymmetries in the yoke contributions to each aperture,

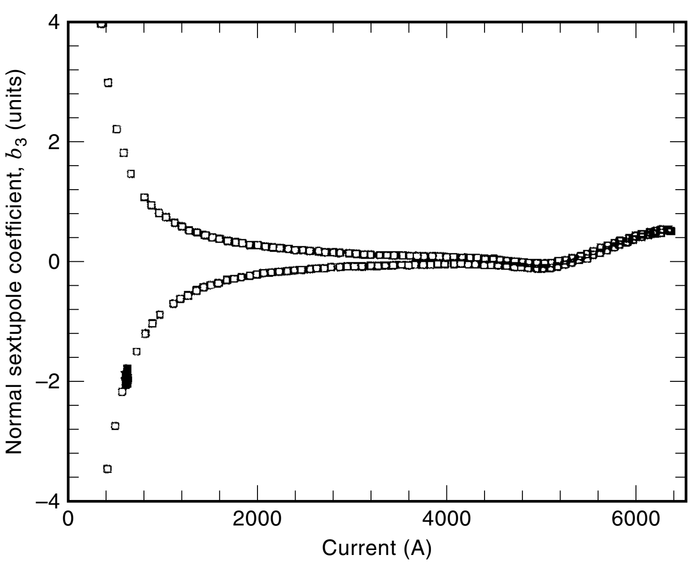

Figure 9. Measurements of normal sextupole coefficient b_3 as a function of current in the central part of a SSC dipole magnet showing the hysteresis resulting from superconductor magnetization and the distortions at high currents resulting from iron saturation.

which affect the normal quadrupole coefficient b_2. The saturation effects in b_2 are of opposite sign in the two apertures.

In any case, the iron contribution depends on the packing factor of the yoke laminations, which must be tightly controlled over the magnet length. Also, the iron yoke must be carefully aligned to limit magnet assembly twist.

Superconductor Magnetization

Critical State Model. According to the so-called critical state model, bipolar magnetization currents are induced at the periphery of the superconducting filaments in the cable strands each time the field to which the filaments are exposed is varied (46). The magnetization currents distribute themselves with a density equal to the superconductor critical current density at the given temperature and field J_C, in order to screen the filament cores from the applied field change. Unlike regular eddy currents, the magnetization currents do not depend on the rate of field variations. Also, because they can flow with zero resistance, they do not decay as soon as the field ramp is stopped. They are called *persistent magnetization currents.*

Effects of Superconductor Magnetization. When an accelerator magnet is cycled in current, the bipolar shells of magnetization currents induced in the filaments behave as small magnetic moments which contribute to—and distort—the central field. The magnetic moments depend on J_C and are proportional to filament diameter. Their distribution follows the symmetries of the transport-current field (i.e., the field produced by the transport current in the magnet coil), and, if the superconductor properties are uniform, only the allowed multipole coefficients are affected. Computer models that can accurately predict the field distortions resulting from superconductor magnetization have been developed (47).

The field distortions are the most significant at low transport current, where the transport-current field is low and J_C is large. They are progressively overcome as the transport-current field increases and J_C diminishes and become negligible at high transport current. They change sign and regain influence as the transport current is ramped down. As a result, the allowed multipole coefficients exhibit sizable hystereses as a function of transport current, which depend on magnet excitation history. This is illustrated in Fig. 9, which shows measurements of b_3 as a function of current in the central part of a SSC dipole magnet. In Fig. 9, the magnetization effects can be seen at currents below 3 kA (as explained in the previous section, the distortions at high field result from iron yoke saturation).

The field distortions resulting from superconductor magnetization are one of the major drawbacks of using supeconducting magnets in a particle accelerator. They can be reduced by reducing filament size (typically, to 5 μm for SSC and LHC strands), but they cannot be eliminated. The powering cycle of the magnets must be adapted to avoid brutal jumps between the two branches of the multipole coefficient hystereses while the beam circulates. Also, elaborate beam optics correction schemes must be developed. This can include superconducting, high-order multipole magnets (chapter 9 of Ref. 2).

Time Decay. In addition, the effects of superconductor magnetization are not indefinitely persistent, but exhibit a slow time decay, which, at low transport current, can result in significant drifts of the allowed multipole coefficients (48,49). These drifts are particularly disturbing during the injection phase of machine operation, where the magnet current is maintained at a constant and low level for some period of time (50). Also, they complicate the early stages of acceleration, for, as the current is increased at the end of injection, the drifting multipoles rapidly snap back to values on the hysteresis curves (51). Part of the observed time decay can be attributed to flux creep in the superconductor (52), but flux creep cannot account for the large drifts obverved after a high current cycle (49). The nature of the other mechanisms that may be involved is not well understood.

Coupling Currents

As described in the conductor section, accelerator magnet coils are wound from Rutherford-type cables, which consist of a few tens of strands twisted together and shaped into a flat, two-layer, slightly keystoned cable. The cable mid-thickness is smaller than twice the strand diameter, which results in strand deformation and large contact surfaces at the crossovers between the strands of the two layers. Furthermore, and as explained in the mechanical design section, the coils are precompressed azimuthally during magnet assembly. Large pressures that keep the strands firmly in contact are thus applied perpendicularly to the cable. The large contact surfaces and the high pressures can result in low contact resistances at the strand crossovers.

In the steady state, the transport current flows in the superconducting filaments, which offer no resistance. When the cable is subjected to a transverse varying field, the network of low interstrand resistances allows the formation of current loops, which are superimposed on the transport current. The loop currents, referred to as *interstrand coupling currents,* circulate along the superconducting filaments and cross over from strand to strand through the interstrand resistances. Unlike persistent magnetization currents, the interstrand coupling currents are directly proportional to the rate of field variations, and they start to decay as soon as the field ramp is stopped.

Interstrand coupling currents have three main effects on magnet performance (39): (1) quench current degradation (for they are superimposed on the transport current), (2) heat dissipation (when crossing the interstrand resistances), and (3) field distortions. This last issue is the most critical for accelerator magnet applications.

The coupling current contribution to the central field does not depend on transport current and increases linearly as a function of current ramp rate. If the interstrand resistance is uniform throughout the coil assembly, the coupling current distribution follows the symmetries of the transport-current field, and only the allowed multipole coefficients are affected. In practice, however, there can be large coil-to-coil differences as well as large nonuniformities within the coils themselves, which result in sizable effects in the unallowed multipole coefficients. This is illustrated in Fig. 10 (a, b), which presents plots of the skew and normal sextupole field coefficients (A_3 and B_3) as functions of current, measured at various ramp rates in the central part of a SSC dipole magnet prototype. (Note that the transport-current contribution has been substracted from the data.) No particular treatment (such as stabnite) was applied to the strands of the cable used in this prototype.

The effects of interstrand coupling currents can be limited by ensuring that the interstrand resistances are not too low. However, and as mentioned in the conductor section, the interstrand resistances should not be too large either to allow some possibility of current redistribution among cable strands.

Longitudinal Periodicity

When measuring the field with fine spatial resolution along the axis of an accelerator magnet, all multipole coefficients appear to exhibit periodic oscillations (53,54). The amplitude of the oscillations varies as a function of space, transport current, excitation history, and time, but the wavelength is always approximately equal to the twist pitch length of the cable used in the innermost coil layer.

The longitudinal periodic oscillations are believed to result from imbalances in the current distribution among cable

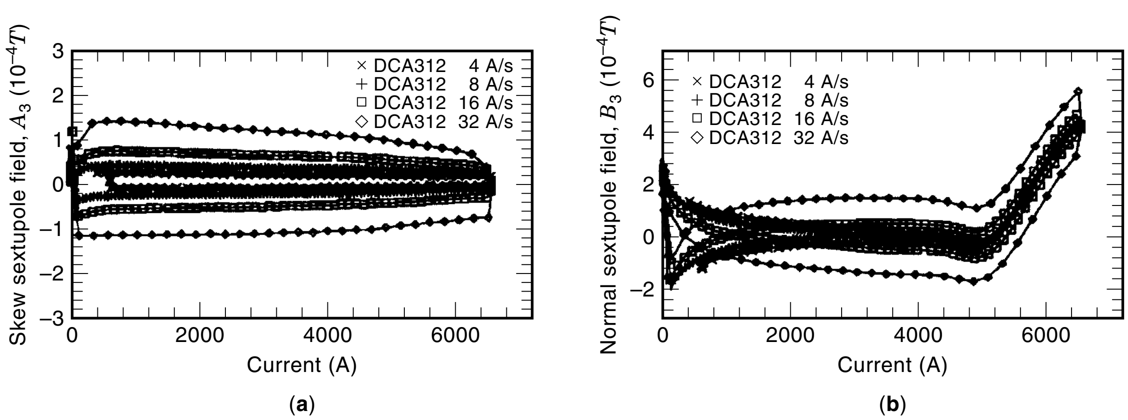

Figure 10. Effects of interstrand coupling currents on multipole field coefficients as measured as a function of ramp rate in the central part of a SSC dipole magnet (39): (a) skew sextupole field coefficient A_3 and (b) normal sextupole field coefficient B_3. The transport-current contribution is subtracted from the data.

strands. The current imbalances may have at least three origins: (1) nonuniformities in the properties of cable strands, (2) nonuniformities in the solder joints connecting the coils in series to the current leads, and (3) large and long-lasting interstrand coupling current loops superimposed on the transport current (55). Such current loops could be induced by spatial variations in the time-derivative of the field to which the cable is exposed as it turns around the coil ends or exits toward the current leads (56–58).

The oscillation wavelength is too short to affect beam optics but may be an issue for magnetic measurements. It is recommended that the measurements be averaged over an integer number of cable pitch lengths. Also, the slow decay of the large interstrand coupling current loops associated with these periodic oscillations may contribute to the drifts of the allowed multipole coefficients observed at low and constant transport current (see the section on superconductor magnetization) (59).

MECHANICAL DESIGN

Support Against the Lorentz Force

Components of the Lorentz Force. The high currents and fields in an accelerator magnet coil produce a large Lorentz force on the conductors. In a dipole coil, the Lorentz force has three main components, which are represented in Fig. 6 (38,60): (1) an azimuthal component, which tends to squeeze the coil toward the coil assembly midplane [which, in the coordinate system defined previously, corresponds, for a dipole magnet, to the horizontal ($\boldsymbol{x}$, $\boldsymbol{z}$) plane], (2) a radial component, which tends to bend the coil outwardly, with a maximum displacement at the coil assembly midplane (along the horizontal x axis for a dipole magnet), and (3) an axial component, arising from the solenoidal field produced by the conductor turnaround at the coil ends and which tends to stretch the coil outwardly (along the z axis).

Stability against Mechanical Disturbances. Because accelerator magnets are operated close to the critical current limit of their cables, their minimum quench energy (MQE), defined as the minimum energy deposition needed to trigger a quench, is very small. As a matter of fact, the MQE of accelerator magnets is of the same order of magnitude as the electromagnetic work produced by minute wire motions in the coil (61). If the motions are purely elastic, no heat is dissipated, and the coil remains superconducting, but if the motions are frictional, the associated heat dissipation may be sufficient to initiate a quench. This leaves two possibilities: either to prevent wire or coil motion by providing a rigid support against the various components of the Lorentz force or to reduce to a minimum the friction coefficients between potentially moving parts of magnet assembly.

Conceptual Design. The mechanical design concepts used in present accelerator magnets are more or less the same and were developed at the time of the Tevatron (4,62). In the radial direction, the coils are confined within a rigid cavity defined by laminated collars, which are locked around the coils by means of keys or tie rods. In the azimuthal direction, the collars are assembled so as to precompress the coils. In the axial direction, the coils either are free to expand or are restrained by means of stiff end plates.

The use of laminated collars, pioneered at the Tevatron, was a real breakthrough in achieving a rigid mechanical support while keeping tight tolerances over magnet assemblies, which are a few meters in length and which must be mass-produced. The laminations are usually stamped by a fine blanking process allowing a dimensional accuracy on the order of one hundredth of a millimeter to be achieved.

Azimuthal Precompression

Preventing Collar Pole Unloading. As described previously, the azimuthal component of the Lorentz force tends to squeeze the coil toward the midplane. At high fields, it may happen that the coil pole turns move away from the collar poles, resulting in variations of the coil pole angle that distort the central field and creating a risk of mechanical disturbances. To prevent conductor displacements, the collars are assembled and locked around the coils so as to apply an azimuthal precompression. The precompression is applied at room temperature and must be sufficient to ensure that, after cool-down and energization, there is still contact between coil pole turns and collar poles.

Precompression Requirement. To determine the proper level of room temperature azimuthal precompression, at least three effects must be taken into account: (1) stress relaxation and insulation creep following the collaring operation, (2) thermal shrinkage differentials between coil and collars during cool-down (if any), and (3) stress redistribution resulting from the azimuthal component of the Lorentz force. In addition, the collaring procedure must be optimized to ensure that the peak pressure seen by the coils during the operation (which may be significantly higher than the residual precompression) does not overstress the insulation (Ref. 60, p. 1326).

The precompression loss during cool-down, $\Delta\sigma$, can be estimated from

$$\Delta\sigma \approx E_{\mathrm{cl}}(\alpha_{\mathrm{cl}} - \alpha_{\mathrm{cr}}) \tag{20}$$

where E_{cl} is the coil Young's modulus in the azimuthal direction, and α_{cl} and α_{cr} are the thermal expansion coefficients of the coil (in the azimuthal direction) and of the collars, integrated between room and operating temperatures. Note that Eq. (20) is derived with the assumptions that E_{cl} does not depend on temperature and that the collars are infinitely rigid.

Choice of Collar Material. To limit cool-down loss, it is preferable to use for the collars a material whose integrated thermal expansion coefficient matches more or less that of the coil. For NbTi coils with polyimide–glass or all-polyimide insulation, this suggests aluminum alloy (see Table 2). How-

Table 2. Integrated Thermal Expansion Coefficients between 4.2 K and Room Temperature (10^{-3} m/m)

Low carbon steel	2.0
Stainless steel (304/316)	2.9
Copper (OFHC)	3.1
Aluminum	4.2
Insulated cable (polyimide/glass)	5.1[a]
Insulated cable (all polyimide)	5.6[a]

[a] Transverse direction; SSC inner cable.

ever, and as will be described in the next section, it is also desirable that the collars be as rigid as possible or have an integrated thermal expansion coefficient approaching that of the low carbon steel used for the yoke. This favors austenitic stainless steel, which has a lower integrated thermal expansion coefficient and whose Young's modulus is 195 GPa at room temperature and 203 GPa at 4.2 K, compared to 72 GPa at room temperature and 80 GPa at 4.2 K for aluminum alloy.

When assessing the respective merits of austenitic stainless steel and aluminum alloy, note that austenitic stainless steel presents a better resistance to stress cycling at low temperature (63), but that it has a higher density (7800 kg/m^3 compared to 2800 kg/m^3 for aluminum alloy) and is more expensive.

There is no ideal choice between stainless steel and aluminum alloy, and magnets with both types of collar materials have been built: HERA dipole magnets and most LHC dipole magnet prototypes use aluminum alloy collars, whereas Tevatron dipole magnets and most SSC dipole magnet prototypes rely on stainless steel collars. In any case, and whichever collar material is chosen, a thorough mechanical analysis of the structure under the various loading conditions is required.

Radial Support

Limiting Radial Deflections. As described previously, the radial component of the Lorentz force tends to bend the coil outwardly, with a maximum displacement at the coil assembly midplane. At high fields, this bending results in shear stresses between coil turns and in an ovalization of the coil assembly (along the horizontal x axis for a dipole magnet), which generates field distortions. To prevent displacements or deformations, the radial deflections of the coil assembly must be limited to, typically, less than 0.05 mm.

Seeking Yoke Support. The main support against the radial component of the Lorentz force is provided by the collars, whose stiffness and radial width must be optimized to limit collared-coil assembly deflections. However, in the magnetic design of high field magnets, the field enhancement provided by the iron yoke is maximized by bringing it as close as possible to the coil. This reduces the space left for the collars, whose rigidity then becomes insufficient to hold the Lorentz force, and the yoke and helium containment shell must also be used as part of the coil support system.

The mechanical design of magnets where the yoke is needed to support the collared-coil assembly is complicated by the fact that the collar material (stainless steel or aluminum) shrinks more during cool-down than the low carbon steel used for the yoke (see Table 2). This thermal shrinkage differential must be compensated for to ensure that, when the magnet is cold and energized, there is a proper contact between the collared-coil assembly and the yoke along the axis of maximum potential displacements. Such contact limits the deformations of the collared-coil assembly and allows a partial transfer (up to 50% in some LHC dipole magnet prototypes) of the radial component of the Lorentz force to the yoke and the shell.

The aforementioned thermal shrinkage differential Δr can be estimated as

$$\Delta r = R_{\mathrm{cr}}(\alpha_{\mathrm{cr}} - \alpha_{\mathrm{yk}}) \tag{21}$$

where R_{cr} is the collar outer radius and α_{yk} is the thermal expansion coefficient of the yoke, integrated between room and operating temperatures.

To limit contact loss due to thermal shrinkage differential, it is preferable to use for the collars a material whose integrated thermal expansion coefficient approaches that of low carbon steel. This suggests the use of austenic stainless steel (see Table 2). However, and as was described in the section on choice of collar material, it is also desirable to limit the cool-down loss of coil precompression, which favors the use of aluminum alloy.

Mechanical Design with Fully Mated Yoke Assembly. To facilitate assembly, the yoke of dipole magnets is usually split into two halves, which are mounted around the collared-coil assembly. The shell, which is also made up of two halves, is then placed around the yoke and welded. If the thermal shrinkage differential between collar and yoke is not too large (as in the case of stainless steel collars), it can be compensated for by designing and assembling the structure so that the two yoke halves apply a compressive load over selected areas of the collared-coil assembly. This compressive load is obtained by introducing a shrinkage allowance into the geometry of either the collars or the yoke and by welding the shell so as to press radially onto the two yoke halves and as to force them to mate at room temperature. During cool-down, the collared-coil assembly shrinks away from the two yoke halves, which remain fully mated. This results in a progressive decrease of the compressive load exerted by the yoke, but a suitable contact can be maintained over the designated areas of the collared-coil assembly.

In practice, the compressive load provided by the yoke is directed along a given axis. The choice of the axis drives the choice of yoke split orientation. The SSC dipole magnet prototypes built at BNL use a horizontally split yoke with a yoke–collar compressive load directed along the vertical y axis as shown in Fig. 11(a), while the SSC dipole magnet prototypes built at FNAL use a vertically split yoke with a yoke–collar compressive load directed along the horizontal x axis as shown in Fig. 11(b) (64). Both types of magnets performed very well.

Mechanical Design with Yoke Midplane Gap at Room Temperature. For large thermal shrinkage differentials (as in the case of aluminum collars), the yoke–collar compressive load required at room temperature for a full compensation would overstress the collared-coil assembly, and a more sophisticated mechanical design must be used. The twin-aperture LHC dipole magnet prototypes with aluminum collars rely on a two-piece, vertically split yoke with an open gap at room temperature and a welded outer shell made of a material (stainless steel or aluminum) that shrinks more during cool-down than the low-carbon steel yoke (65).

In these magnets, the yoke is designed so that, when placed around the collared-coil assembly at room temperature with no pressure applied to it, there remains an opening between the two yoke halves of the order of the expected thermal shrinkage differential. The yoke midplane gap is then closed in two stages: (1) during shell welding, as a result of the compressive load arising from weld shrinkage, and (2) during cool-down, as a result of the compressive load arising from thermal shrinkage differential between yoke and shell.

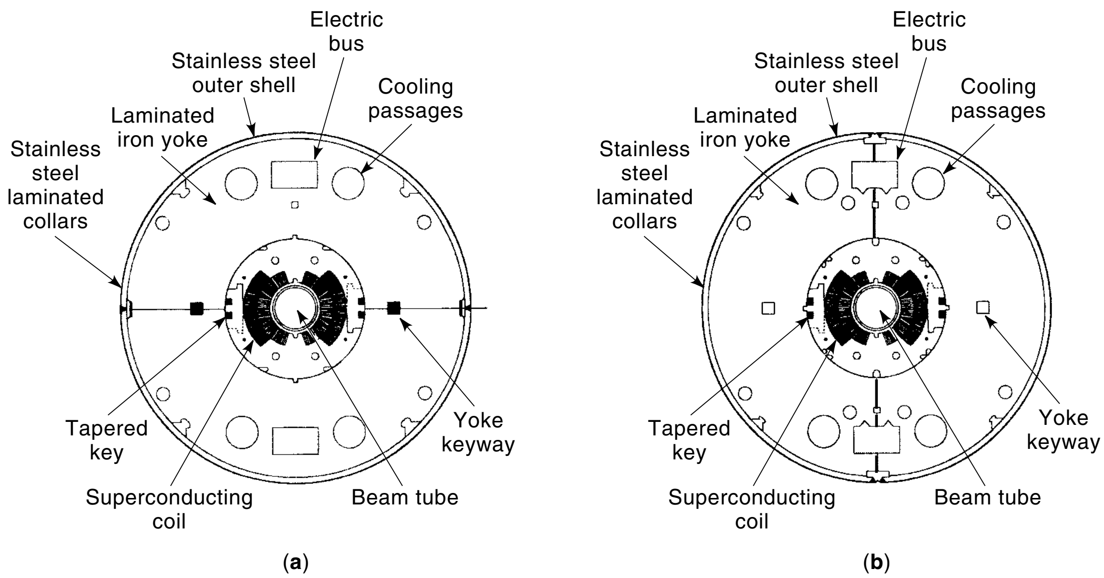

Figure 11. SSC dipole magnet cross-sections (64): (a) BNL-style with horizontally split yoke and (b) FNAL-style with vertically split yoke.

The initial gap closure during shell welding is limited to avoid overstressing the collared-coil assembly. The closure is completed during cool-down thanks to the radial pressure exerted by the shell, which forces the two yoke halves to follow the shrinkage of the collared-coil assembly and to maintain contact along the horizontal x axis. The yoke midplane gap must be fully closed at the end of cool-down to ensure that the structure is very rigid and to avoid any risk of oscillation during energization.

A crucial issue in such a design is the ability to perform the shell welding operation in a reproducible way during mass production so as to achieve the desired yoke midplane gap value at room temperature and to keep a tight tolerance on this value (of the order of 0.1 mm). As we have seen, a gap too close may result in coil overstressing at room temeprature, whereas a gap too open may result in contact loss during cool-down.

In some LHC prototypes, the closure of the yoke midplane gap is controlled by means of aluminum spacers located between the two yoke halves (66). The spacers are dimensioned to have a spring rate similar to that of the collared-coil assembly, and they prevent the gap from closing at room temperature. During cool-down, however, they shrink more than the yoke and cease to be effective.

RHIC Magnets. In RHIC magnets, collar and yoke designs are altogether simplified by replacing the collars by reinforced plastic spacers and by using directly the yoke to precompress the one-layer coils (67). It remains to be seen if this structure could be scaled up to higher-field magnets.

End Support

As described previously, the axial component of the Lorentz force tends to stretch the coil outwardly along the z axis. In magnets where the yoke is not needed to support the collared-coil assembly, a clearance can be left between the two. If the axial stresses resulting from the Lorentz force do not exceed the yield stress of the coil, it is possible to let the collared-coil assembly expand freely within the iron yoke. This is the case of the quadrupole magnets designed at Commissariat à l'Energie Atomique/Saclay for HERA, SSC and LHC (68). However, in magnets where there is contact between collar and yoke, it is essential to prevent stick/slip motions of the laminated collars against the laminated yoke and to provide a stiff support against the axial component of the Lorentz force (60,69). The ends of SSC and LHC dipole magnet coils are contained by thick stainless steel end plates welded to the shell.

MAGNET COOLING

Superconductor Critical Temperature

The superconducting state exists only at temperatures below the so-called *critical temperature* T_C. For NbTi, T_C can be estimated as a function of applied magnetic flux density B using

$$T_C(B) = T_{C0}\left(1 - \frac{B}{B_{C20}}\right)^{1.7} \tag{22}$$

where T_{C0} is the critical temperature at zero field (about 9.2 K) and B_{C20} is the upper critical magnetic flux density at zero temperature (about 14.5 T).

Boiling and Supercritical Helium Cooling. To achieve low temperatures and ensure stable operations against thermal disturbances, the accelerator magnet coils are immersed in liquid helium (70). Helium is a cryogenic fluid whose pressure-temperature phase diagram is presented in Fig. 12. Its boiling temperature is 4.22 K at 1 atm (1 atm ≈ 0.1 MPa).

Small superconducting magnet systems usually rely on boiling helium at 1 atm (71). Boiling helium offers the advantage that, as long as the two phases are present, the temperature is well determined. However, in large-scale applications,

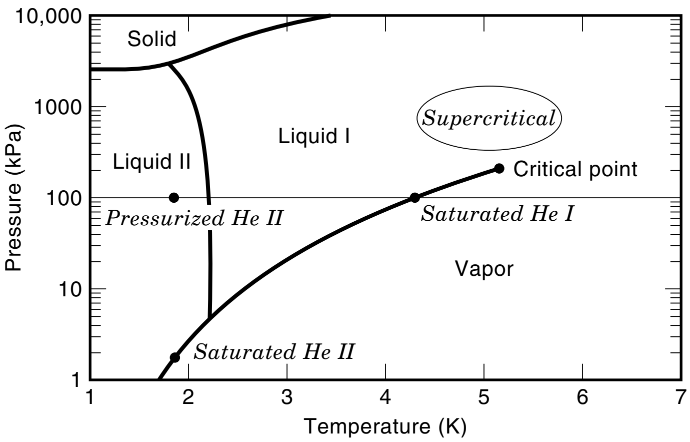

Figure 12. Pressure-temperature phase diagram of helium (71).

such as superconducting particle accelerators, the fluid is forced to flow through numerous magnet cryostats and long cryogenic lines, where heat leaks are unavoidable. The heat leaks result in increases in vapor contents and create a risk of gas pocket formation that may block circulation.

The aforementioned difficulty can be circumvented by taking advantage of the fact that helium exhibits a critical point at a temperature of 5.2 K and a pressure of 0.226 MPa (see Fig. 12). For temperatures and pressures beyond the critical point, the liquid and vapor phases become indistinguishable. The single-phase fluid, which is called *supercritical,* can be handled in a large system without risk of forming gas pockets. However, its temperature, unlike that of boiling helium, is not constant and may fluctuate as the fluid circulates and is subjected to heat losses.

The cryogenic systems of the Tevatron, HERA, and RHIC, and that designed for the SSC, combine single-phase and two-phase helium (71). In the case of the Tevatron and HERA, the insides of the magnet cold masses are cooled by a forced flow of supercritical helium, while two-phase helium is circulated in a pipe running at the cold mass periphery (around the collared-coil assembly for Tevatron magnets, in a bypass hole in the iron yoke for HERA magnets). In the case of the SSC, it was planned to only circulate supercritical helium through the magnet cold masses, while *recoolers,* consisting of heat exchangers using two-phase helium as primary fluid, would have been implemented at regular intervals along the cryogenic lines. The cryogenic system used for the RHIC is inspired by that of the SSC. In all these schemes, the boiling liquid is used to limit temperature rises in the single-phase fluid.

Superfluid Helium Cooling

A peculiarity of helium is the occurrence of *superfluidity* (70). When boiling helium is cooled down at 1 atm, it stays liquid until a temperature of the order of 2.17 K, where a phase transition appears. For temperatures below 2.17 K (at 1 atm) helium loses its viscosity and becomes a superconductor of heat. This property, unique to helium, is called superfluidity. Superfluidity is very similar to superconductivity, except that, instead of electrical conductibility, it is the thermal conductibility that becomes infinite. The transition temperature between the liquid and superfluid phases depends on pressure. It is called the *lambda temperature* T_λ.

The LHC magnets are cooled by superfluid helium, and their operating temperature is set at 1.9 K (72). Decreasing the temperature improves the current-carrying capability of NbTi dramatically and allows higher fields to be reached. (For NbTi, the curve of critical current density as a function of field is shifted by a about +3 T when lowering the temperature from 4.2 K to 1.9 K.) The feasibility of a large-scale cryogenic installation relying on superfluid helium has been demonstrated by Tore Supra, a superconducting tokamak built at Commissariat à l'Energie Atomique/Cadarache near Aix en Provence in the South of France and operating reliably since 1988 (73).

Magnet Cryostat

To maintain the magnet cold masses at low temperature, it is necessary to limit heat losses. There are three mechanisms of heat transfer (74): (1) convection, (2) radiation, and (3) conduction. The convection losses are eliminated by mounting the cold masses into cryostats, which are evacuated (71,75). The radiation losses, which scale in proportion with the effective emissivities of the surfaces facing each other and with the fourth power of their temperatures, are reduced by surrounding the cold masses with blankets of multilayer insulation and thermal shields at intermediate temperatures. The main sources of conduction losses are the support posts, the power leads, and the cryogenic feedthroughs, which are designed to offer large thermal resistances.

QUENCH PERFORMANCE

As explained in the operating margin section, the maximum quench current I_{qm} of a magnet at a given operating temperature can be estimated from the critical current of the cable and the peak field on the coil. It corresponds to the ultimate current-carrying capability of the cable and can be raised only by lowering the operating temperature.

When energizing a superconducting magnet, the first quenches usually occur at currents below I_{qm} (chapter 5 of Ref. 76). In most cases, however, it appears that, upon sucessive energizations, the quench currents gradually increase. This gradual improvement is called the magnet's *training.* The training often leads to a stable *plateau* corresponding to the maximum quench current.

Quenches below the expected maximum quench current have at least four origins: (1) energy deposition in the magnet coil resulting from frictional motions under the Lorentz force, (2) energy deposition from synchrotron radiation and beam losses, (3) heat dissipation from coupling currents in the cable, and (4) current imbalances among cable strands. Quenches of the first origin reveal flaws in the mechanical design or in the assembly procedures that must be analyzed and corrected. The effects of synchrotron radiation can be reduced by implementing an intercepting screen within the beam tube. Coupling losses and current imbalances are only of concern for fast current cycles.

When operating an accelerator made up of several hundred or even several thousand superconducting magnets, it cannot be tolerated that magnets quench at random. Hence, the magnets must be designed with a safe margin above the maximum operating current of the machine. In addition, systematic tests must be carried out before installing the magnets in the tunnel to ensure that their quench performance is adequate and does not degrade upon extended current and thermal cycling (77).

QUENCH PROTECTION

Conductor Heating

Although most R&D programs have been successful in developing magnet designs that can be mass-produced and meet accelerator requirements, quenches do occur in accelerator operations. These quenches must be handled in order to avoid any damage of the quenching magnet, to ensure the safety of the installation, and to minimize down time.

The most damaging effect of a quench is that, once a volume of conductor has switched to the normal resistive state, it dissipates power by the Joule effect (Chapter 9 of Ref. 76). Most of this power is consumed locally in heating up the conductor. In a very short time (typically a few tenths of a second), the conductor temperature can reach room temperature, and, if the magnet is not discharged, keep on increasing.

Maximum-Temperature Requirement. The temperature rise subsequent to a quench must be limited for at least three reasons: (1) to restrict the thermal stresses induced in the quenching coil, (2) to prevent degradation of superconductor properties, and (3) to avoid insulation damage.

For most materials, thermal expansion starts to be significant for temperatures above 100 K. The critical current density of NbTi is affected by exposure to temperatures above 250°C. The extent of degradation depends on the temperature level and on the duration of the exposure: at 250°C, it takes of the order of 1 h for significant degradation to occur, while it may take less than a minute at 400°C to 450°C (78). Finally, the polyimide materials used to insulate NbTi cables lose most of their mechanical properties for temperatures above 500°C.

It follows that an upper limit for conductor heating subsequent to a quench is 400°C. Most magnets are designed not to exceed 300 K to 400 K, and whenever possible, the limit should be set at 100 K.

Protecting a Quenching Magnet

The source of conductor heating in a quenching magnet is power dissipation by the Joule effect. Power keeps being dissipated as long as there is current in the magnet coil. To eliminate the heat source and limit the temperature rise, it is thus necessary to ramp the current down.

To discharge a quenching magnet, all its stored magnetic energy must be converted into resistive power. If the zone where the conductor has switched to the normal state remains confined to a small volume, there is a risk that a large fraction of the stored energy will be dissipated in this small volume. In the case of a string of magnets connected electrically in series, it may even happen that the energy of the whole string will be dissipated in the quenching magnet. Hence, to prevent burnout, it is necessary to ensure that the normal resistive zone spreads rapidly throughout the quenching coil. This can be done by means of heaters, implemented near the magnet coils and fired as soon as a quench is detected. These heaters are referred to as *quench protection heaters.*

In comparison with other superconducting magnets, most accelerator magnets require an active quench protection system because of the rapidity of the temperature rise resulting from the high current density and the low fraction of stabilizing copper in the cable strands. One notable exception is the RHIC dipole magnets, whose one-layer coil assemblies are wound from a cable with a high copper-to-superconductor ratio (2.25 to 1), and which do not rely on quench protection heaters.

Hot Spot Temperature

Estimating Hot Spot Temperature. The volume of conductor that heats up the most significantly during a quench is the spot where the quench first originated. It is called the *hot spot.* An upper limit of the hot spot temperature, $T_{\max}$, can be determined by assuming that, near the hot spot, all the power dissipated by the Joule effect is used to heat up the conductor. Integrating the heat balance equation yields

$$S^2 \int_{T_0}^{T_{\max}} dT \frac{C(T)}{\rho(T)} = \int_{t_0}^{+\infty} dt\, I(t)^2 \tag{23}$$

where C is the overall specific heat per unit volume of conductor, ρ is the overall conductor resistivity in the normal state, S is the conductor cross-sectional area, I is the current, t_0 is the time of quench start, and T_0 is the coil temperature at t_0.

The left member of Eq. (23) depends only on conductor properties whereas the right member depends only on the characteristics of current decay. The right-hand side integral, divided by 10^6, is called the *MIIT integral* (Mega I times I versus Time integral) and its value is refered to as the *number of MIITs.* The maximum temperatures computed from the numbers of MIITs have been shown to be in fairly good agreement with actual measurements of hot spot temperatures on quenching magnets (79).

Limiting Hot Spot Temperature. The hot spot temperature can be limited by acting on either member of Eq. (23). Regarding the left member, the only conceivable action is to reduce the overall conductor resistivity by increasing the copper-to-superconductor ratio. However, and as explained in the conductor section, the copper-to-superconductor ratio must also be optimized to ensure a high overall critical current. Regarding the right member, the MIIT integral can be minimized by (1) detecting the quench as soon as possible, (2) turning off the power supply (case of a single magnet) or forcing the current to bypass the quenching magnet (case of a magnet string), (3) firing the quench protection heaters, and (4) discharging the quenching magnet or the magnet string.

Quench Detection

The magnets are connected to quench detection systems that monitor the occurrence of a resistive voltage in the coil windings or the coils leads. The resistive voltage must be discriminated from inductive voltages arising from magnet ramping. The inductive components are cancelled out by considering voltage differences across two identical coil assemblies or two identical parts of a given coil assembly (e.g., the upper and lower half coils in a dipole magnet). When the resistive voltage exceeds a preset threshold over a time exceeding a preset duration, the detection system generates a trigger that signals the occurrence of a quench.

Protection of a Single Magnet

Current Decay. Let us first consider the case of a single magnet, and let us assume that, once a quench is detected, the power supply is turned off and the magnet is switched to an external dump resistor, R_{ext}. The current decay is determined by

$$L_{m}\frac{dI}{dt}+[R_{q}(t)+R_{ext}]I=0 \tag{24}$$

where L_m is the magnet inductance and $R_q(t)$ is the developing resistance in the quenching coils. Furthermore, the total voltage across the magnet V_m is given by

$$V_{m}=R_{e}I(t) \tag{25}$$

where I is the current intensity.

To limit the number of MIITs, it is desirable to have a fast current decay. Equation (24) shows that fast decay rates are obtained either by means of a large R_e or by ensuring that $R_q(t)$ increases rapidly. For some magnets, an external resistor can be used to extract a significant fraction of the stored magnetic energy. However, it is also required to keep V_m to a reasonable level (typically less than 1 kV) to avoid insulation breakdown. Given the order of magnitude of I (up to 15 kA), this imposes a small R_e (typically a few hundredths of an ohm), which, during a quench, is soon overcome by $R_q(t)$. Hence, for accelerator magnets, the current decay is largely dominated by the resistance development in the quenching coils, and the decay rate can be increased only by speeding up $R_q(t)$.

Maximum Voltage to Ground. The developing resistance in the quenching coil separates the coil impedance into several parts (Ref. 2, p. 137): unquenched parts across which the voltage is mainly inductive and quenched parts across which the voltage is mainly resistive. The resistive and inductive voltages compensate each other partially so that their sum equals V_m. The voltage distribution with respect to ground depends on the respective sizes and locations of these various parts. The more uniform the quench development, the lower the maximum voltage to ground. As an illustration, Fig. 13 shows the voltage distribution in a quenching magnet. Here, V_m is assumed to be nil, and R_q is assumed to be concentrated near two-thirds of the magnet length.

Quench Protection Heaters. As described earlier, to speed up and uniformize quench development, most accelerator magnets rely on quench protection heaters, which are fired as soon as a quench is detected. The heaters are usually made of stainless steel strips, which are copper clad at regular intervals along their lengths and which are placed on the outer surface of the coil assemblies. Note, however, that the heater firing unit relies on a capacitor bank and that it takes some time for the energy to be released. Note also that the heaters must be electrically insulated from the coil and that this electrical insulation introduces a thermal barrier. As a result, there is a nonnegligible delay between the firing of the heaters and their effect on the coils, during which we must rely on natural quench propagation (80). The heaters and their implementations in the magnet assembly are optimized to reduce this delay.

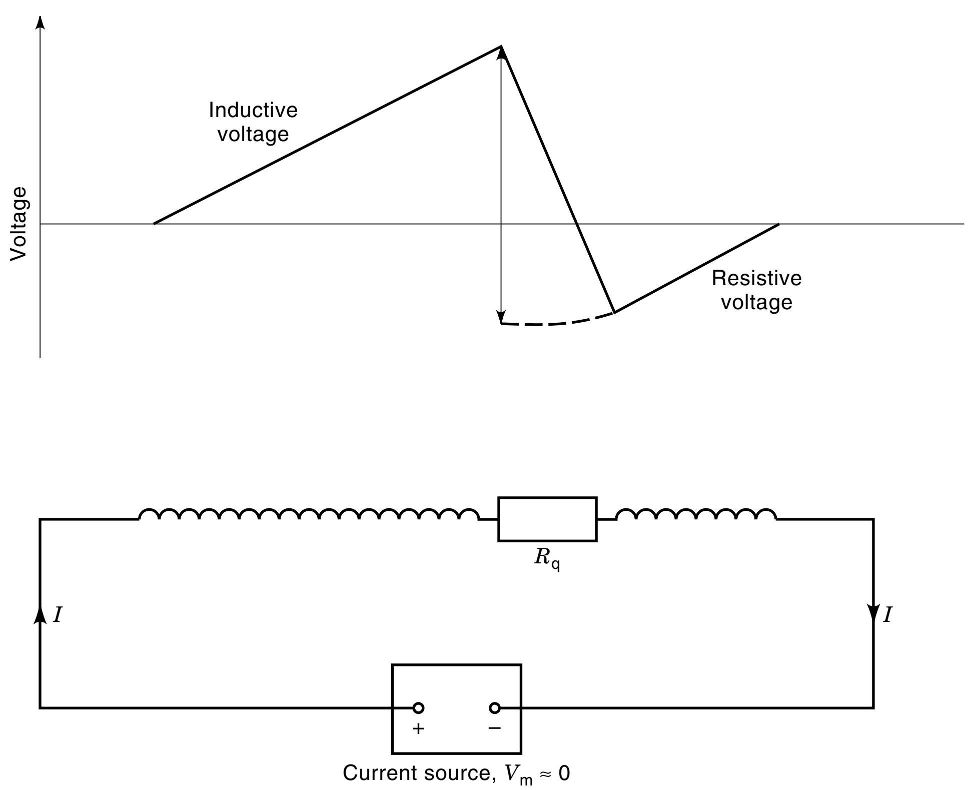

Figure 13. Voltage distribution in a quenching magnet. The total voltage across the magnet is assumed to be nil and the developing resistance is assumed to be concentrated near two-thirds of the magnet length (2).

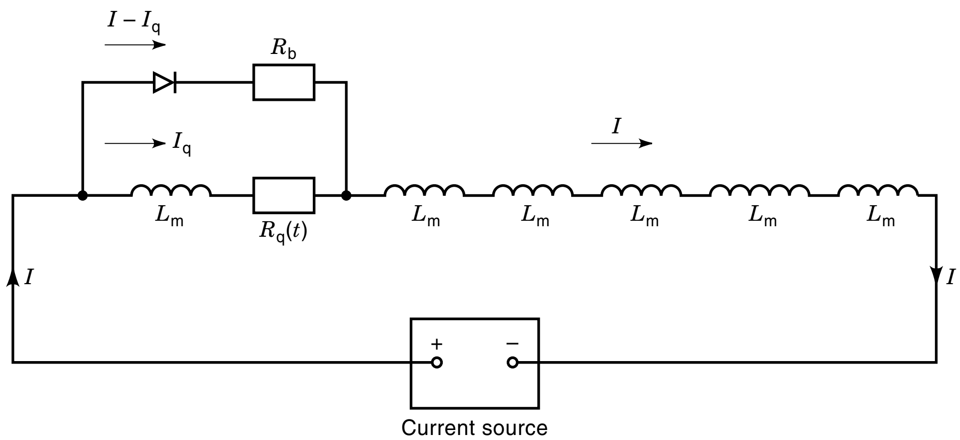

Figure 14. Electrical circuit of a quenching magnet in a magnet string (2).

Protection of a Magnet String

In an accelerator, the magnet ring is divided into several sectors made up of series-connected magnets. The sectors are powered independently and are electrically independent. Once a quench is detected in a magnet, the power supply of the sector to which the magnet belongs is turned off and the sector is discharged over a dump resistor.

Unlike in the case of a single magnet, the current decay rate in the sector must be limited for at least two reasons: (1) to prevent the induction of large coupling currents in the magnet coils (which may quench the remaining magnets in the sector, resulting in general warming and significant helium venting) and (2) to avoid the occurrence of unacceptable voltages to ground (because of the large overall inductance of the sector). A too slow decay rate, however, creates the risk that a significant fraction of the total energy stored in the sector be dissipated in the quenching magnet, resulting in destructive overheating.

These contradictory considerations can be reconciled by forcing the current to bypass the quenching magnet and by ramping the current down at the desired rate in the remaining unquenched magnets. The bypass elements consist of diodes (or thyristors) connected in parallel to individual or small groups of magnets, as shown in Fig. 14. As long as the magnets are superconducting, the current flows through the magnets. Once a magnet has quenched and starts to develop a resistive voltage, the main current is bypassed through the diode connected in parallel, and the quenching magnet is discharged over the diode circuit. The current decay is determined by an equation similar to Eq. (24), except that R_e must be replaced by the resistance associated with the bypass element R_b.

HERA, RHIC, and LHC rely on silicon diodes that are mounted inside the helium cryostats and operate at cryogenic temperatures. The main requirements for these cold diodes are (81): (1) small forward voltage and low dynamic resistance (to limit power dissipation in the diodes), (2) good radiation hardness, and (3) large backward voltage. In the case of the Tevatron, which has a short current ramp time resulting in large inductive voltages across the bypass elements, the diodes are replaced by thyristors operating as fast switches (82). The thyristors are located outside the magnet cryostats and require additional power leads and cryogenic feedthroughs.

The protection system of the magnet ring must be carefully designed and thoroughly tested before starting up the machine. The system tests are usually carried out on a cell or a half-cell representative of the magnet lattice, and all failure modes are investigated (83–85).

SUMMARY

As of today, two large superconducting accelerator rings, Tevatron and HERA, have been built and are reliably operating, and work is under way on two other superconducting colliders—RHIC and LHC. The construction of RHIC is near completion, and the industrial contracts for the mass production of LHC magnets will be awarded in 1999.

Since the time of the Tevatron (late 1970s), a factor of about two has been gained on the critical current density of NbTi at 4.2 K and 5 T, and a dipole field of 10.5 T has been reached on a short magnet model relying on NbTi cables at 1.8 K. In recent years, encouraging results have been obtained on a couple of short dipole magnet models relying on Nb_3Sn cables, which may open the range 10 T to 15 T.

BIBLIOGRAPHY

1. D. A. Edwards and M. J. Syphers, *An Introduction to the Physics of High Energy Particle Accelerators,* New York: Wiley, 1993.
2. K.-H. Mess, P. Schmüser, and S. Wolf, *Superconducting Accelerator Magnets,* Singapore: World Scientific, 1996.
3. H. T. Edwards, The Tevatron energy doubler: A superconducting accelerator, *Annu. Rev. Nucl. Part. Sci.,* **35**: 605–660, 1985.
4. A. V. Tollestrup, Superconducting magnets, *AIP Conf. Proc.,* **87**: 1982, pp. 699–804.
5. B. H. Wiik, The status of HERA, *Conf. Rec. 1991 IEEE Part. Accel. Conf.,* IEEE Catalogue 91CH3038-7, 1991, pp. 2905–2909.
6. R. Meinke, Superconducting magnet system for HERA, *IEEE Trans. Magn.,* **27**: 1728–1734, 1991.
7. V. I. Balbekov and G. G. Gurov, IHEP accelerating and storage complex: Status and possibility of B-factory, *Nucl. Instrum. Meth. Phys. Res., A* **333**: 189–195, 1993.
8. A. V. Zlobin, UNK superconducting magnets development, *Nucl. Instrum. Meth. Phys. Res., A* **333**: 196–203, 1993.
9. R. F. Schwitters, Future hadron collider: The SSC, *AIP Conf. Proc.,* **272**: 1993, pp. 306–320.

10. R. I. Schermer, Status of superconducting magnets for the superconducting super collider, *IEEE Trans. Magn.,* **30**: 1587–1594, 1994.

11. H. Foelsche et al., The relativistic heavy ion collider, RHIC, in H. Schopper (ed.), *Advances of Accelerator Physics and Technologies,* vol. 12, Adv. Ser. Directions High Energy Phys., Singapore: World Scientific, 1993, pp. 104–131.

12. A. Greene et al., The magnet system of the relativistic heavy ion collider (RHIC), *IEEE Trans. Magn.,* **32**: 2041–2046, 1996.

13. L. R. Evans, The large hadron collider project, in T. Haruyama, T. Mitsui, and K. Yamafuji (eds.), *Proc. 16th Int. Cryogenic Eng. Conf./Int. Cryogenic Mater. Conf.,* London: Elsevier, 1997, pp. 45–52.

14. R. Perin, Status of LHC programme and magnet development, *IEEE Trans. Appl. Supercond.,* **5**: 189–195, 1995.

15. M. N. Wilson, Superconducting magnets for accelerators: A review, *IEEE Trans. Appl. Supercond.,* **7**: 727–732, 1997.

16. A. den Ouden et al., Application of Nb_3Sn superconductors to high-field accelerator magnets, *IEEE Trans. Appl. Supercond.,* **7**: 733–738, 1997.

17. R. M. Scanlan et al., Preliminary test results of a 13 tesla niobium tin dipole, *Inst. Phys. Conf. Ser.,* **158**: 1503–1506, 1997.

18. E. Gregory, Conventional wire and cable technology, *AIP Conf. Proc.,* **249**: part 2, 1992, pp. 1198–1229.

19. L. Bottura, private communication, 1997.

20. D. C. Larbalestier and P. J. Lee, New development in niobium titanium superconductors, *Proc. 1995 IEEE Part. Accel. Conf.,* vol. 2, 1995, pp. 1276–1281.

21. D. Leroy et al., Design features and performance of a 10 T twin aperture model dipole for LHC, *Proc. 15th Int. Conf. Magn. Technol.* (MT-15), Beijing, China, 1997, submitted.

22. L. T. Summers et al., A model for the prediction of Nb_3Sn critical current as a function of field, temperature, strain and radiation damage, *IEEE Trans. Magn.,* **27**: 2041–2044, 1991.

23. R. Aymar, Overview of the ITER project, in T. Haruyama, T. Mitsui, and K. Yamafuji (eds.), *Proc. 16th Int. Cryogenic Eng. Conf./Int. Cryogenic Mater. Conf.,* London: Elsevier, 1997, pp. 53–59.

24. P. Bruzzone et al., Testing of industrial Nb_3Sn strands for high field fusion magnets, *IEEE Trans. Magn.,* **30**: 1986–1989, 1994.

25. D. C. Larbalestier, The road to conductors of high temperature superconductors: 10 years do make a difference!, *IEEE Trans. Appl. Supercond.,* **7**: 90–97, 1997.

26. J. M. Royet and R. M. Scanlan, Manufacture of keystoned flat superconducting cables for use in SSC dipoles, *IEEE Trans. Magn.,* **MAG-23**: 480–483, 1987.

27. M. N. Wilson and R. Wolf, Calculation of minimum quench energies in Rutherford-type cables, *IEEE Trans. Appl. Supercond.,* **7**: 950–953, 1997.

28. A. K. Ghosh, W. B. Sampson, and M. N. Wilson, Minimum quench energies of Rutherford cables and single wires, *IEEE Trans. Appl. Supercond.,* **7**: 954–957, 1997.

29. T. Shintomi et al., Development of large keystone angle cable for dipole magnet with ideal arch structure, *Adv. Cryog. Eng. (Mater.),* **36** (A): 323–328, 1990.

30. R. M. Scanlan and J. M. Royet, Recent improvements in superconducting cable for accelerator dipole magnets, *Conf. Rec. 1991 IEEE Part. Accel. Conf.,* 1991, pp. 2155–2157.

31. D. Richter et al., DC measurements of electrical contacts between strands in superconducting cables for the LHC magnets, *IEEE Trans. Appl. Supercond.,* **7**: 786–792, 1997.

32. J. M. Depond et al., Examination of contacts between strands by electrical measurement and topographical analysis, *IEEE Trans. Appl. Supercond.,* **7**: 793–796, 1997.

33. J. D. Adam et al., Rutherford cables with anisotropic transverse resistance, *IEEE Trans. Appl. Supercond.,* **7**: 958–961, 1997.

34. R. A. Haarman and K. D. Williamson, Jr., Electrical breakdown and tracking characteristics of pulsed high voltages in cryogenic helium and nitrogen, *Adv. Cryog. Eng.,* **21**: 102–108, 1975.

35. P. Védrine et al., Mechanical tests on the prototype LHC lattice quadrupole, *IEEE Trans. Magn.,* **30**: 2475–2478, 1994.

36. M. Anerella et al., Improved cable insulation for superconducting magnets, *Proc. 1993 Part. Accel. Conf.,* 1993, pp. 2790–2792.

37. G. H. Morgan, Shaping of magnetic fields in beam transport magnets, *AIP Conf. Proc.,* **249**: part 2, 1992, pp. 1242–1261.

38. R. C. Gupta, S. A. Kahn, and G. H. Morgan, SSC 50 mm dipole cross section, in J. Nonte (ed.), *Supercollider 3,* New York: Plenum, 1991, pp. 587–599.

39. A. Devred and T. Ogitsu, Ramp-rate sensitivity of SSC dipole magnet prototypes, in S. I. Kurokawa, M. Month, and S. Turner (eds.), *Frontiers of Accelerator Technology,* Singapore: World Scientific, 1996, pp. 184–308.

40. H. H. J. ten Kate et al., The reduction of the critical current in Nb_3Sn cables under transverse forces, *IEEE Trans. Magn.,* **28**: 715–718, 1992.

41. R. C. Gupta, A common coil design for high field 2-in-1 accelerator magnets, *Conf. Rec. 1997 IEEE Part. Accel. Conf.,* in press.

42. J. M. Cook, Strain energy minimization in SSC magnet winding, *IEEE Trans. Magn.,* **27**: 1976–1980, 1991.

43. J. S. Brandt et al., Coil end design for the SSC collider dipole magnet, *Conf. Rec. 1991 IEEE Part. Accel. Conf.,* 1991, pp. 2182–2184.

44. T. Garavaglia et al., Application of the SSCRTK numerical simulation program to the evaluation of the SSC magnet aperture, in M. MacAshan (ed.), *Supercollider 2,* New York: Plenum, 1990, pp. 59–76.

45. T. Ogitsu and A. Devred, Influence of azimuthal coil size variations on magnetic field harmonics of superconducting particle accelerator magnets, *Rev. Sci. Instrum.,* **65** (6): 1998–2005, 1994.

46. C. P. Bean, Magnetization of high-field superconductors, *Rev. Mod. Phys.,* **36** (1): 31–39, 1964.

47. H. Brück et al., Field distortions from persistent magnetization currents in the superconducting HERA magnets, *Z. Phys. C—Part. Fields,* **44**: 385–392, 1989.

48. R. W. Hanft et al., Studies of time dependent field distortions from magnetization currents in Tevatron superconducting dipole magnets, *IEEE Trans. Magn.,* **25**: 1647–1651, 1989.

49. A. Devred et al., Time decay measurements of the sextupole component of the magnetic field in a 4-cm aperture, 17-m-long SSC dipole magnet prototype, *Conf. Rec. 1991 IEEE Part. Accel. Conf.,* 1991, pp. 2480–2482.

50. F. Willeke and F. Zimmermann, The impact of persistent current field errors on the stability of the proton beam in the HERA proton ring, *Conf. Rec. 1991 IEEE Part. Accel. Conf.,* 1991, pp. 2483–2487.

51. L. Bottura, L. Walckiers, and R. Wolf, Field errors decay and "snap-back" in LHC model dipoles, *IEEE Trans. Appl. Supercond.,* **7**: 602–605, 1997.

52. P. W. Anderson, Flux creep in hard superconductors, *Phys. Rev. Lett.,* **9** (7): 309–311, 1962.

53. H. Brück et al., Observation of a periodic pattern in the persistent-current fields of the superconducting HERA magnets, *Conf. Rec. 1991 IEEE Part. Accel. Conf.,* 1991, pp. 2149–2151.

54. A. K. Ghosh et al., Axial variations in the magnetic field of superconducting dipoles and quadrupoles, *Proc. 1993 Part. Accel. Conf.,* 1993, pp. 2742–2743.

55. A. Akhmetov et al., Current loop decay in Rutherford-type cables, in P. Hale (ed.), *Supercollider 5,* New York: Plenum, 1994, pp. 443–446.

56. L. Krempanski and C. Schmidt, Influence of a longitudinal variation of dB/dt on the magnetic field distribution of superconducting accelerator magnets, *Appl. Phys. Lett.,* **66** (12): 1545–1547, 1995.

57. A. P. Verweij, Boundary-induced coupling currents in a 1.3 m Rutherford-type cable due to a locally applied field change, *IEEE Trans. Appl. Supercond.,* **7**: 270–273, 1997.

58. L. Bottura, L. Walckiers, and Z. Ang, Experimental evidence of boundary induced coupling currents in LHC prototypes, *IEEE Trans. Appl. Supercond.,* **7**: 801–804, 1997.

59. R. Stiening, private communication, 1991.

60. A. Devred et al., About the mechanics of SSC dipole magnet prototypes, *AIP Conf. Proc.,* **249** (2): 1992, pp. 1309–1374.

61. T. Ogitsu, K. Tsuchiya, and A. Devred, Investigation of wire motion in superconducting magnets, *IEEE Trans. Magn.,* **27**: 2132–2135, 1991.

62. K. Koepke et al., Fermilab doubler magnet design and fabrication techniques, *IEEE Trans. Magn.,* **MAG-15**: 658–661, 1979.

63. D. Perini et al., Measurements of the resistance to stress cycling at 4.2 K of LHC dipole collars, *IEEE Trans. Magn.,* **30**: 1754–1757, 1994.

64. A. Devred et al., Review of SSC dipole magnet mechanics and quench performance, in J. Nonte (ed.), *Supercollider 4,* New York: Plenum, 1992, pp. 113–136.

65. D. Leroy et al., Structural analysis of the LHC 10 T twin-aperture dipole, in T. Sekiguchi and S. Shimamoto (eds.), *Proc. 11th Int. Conf. Magn. Technol.,* London: Elsevier Applied Science, 1990, pp. 159–164.

66. E. Acerbi et al., Development and fabrication of the first 10 m long superconducting dipole prototype for the LHC, *IEEE Trans. Magn.,* **30**: 1793–1796, 1994.

67. P. Wanderer et al., Construction and testing of arc dipoles and quadrupoles for the relativistic heavy ion collider (RHIC) at BNL, *Proc. 1995 Part. Accel. Conf.,* 1995, pp. 1293–1297.

68. J. M. Baze et al., Design and fabrication of the prototype superconducting quadrupole for the CERN LHC project, *IEEE Trans. Magn.,* **28**: 335–337, 1992.

69. J. Strait et al., Tests of full scale SSC R&D dipole magnets, *IEEE Trans. Magn.,* **25**: 1455–1458, 1989.

70. S. W. Van Sciver, *Helium Cryogenics,* New York: Plenum, 1986.

71. P. Lebrun, Cryogenic systems for accelerators, in S. I. Kurokawa, M. Month, and S. Turner (eds.), *Frontiers of Accelerator Technology,* Singapore: World Scientific, 1996, pp. 681–700.

72. P. Lebrun, Superfluid helium cryogenics for the large hadron collider project at CERN, *Cryogenics,* ICEC Suppl., **34**: 1–8, 1994.

73. G. Claudet and R. Aymar, Tore supra and He II cooling of superconducting magnets, *Adv. Cryog. Eng.,* **35** (A): 55–67, 1990.

74. W. Frost (ed.), *Heat Transfer at Low Temperatures,* New York: Plenum, 1975.

75. T. H. Nicol, Cryostat design for the superconducting super collider, *AIP Conf. Proc.,* **249**: part 2, 1992, pp. 1230–1241.

76. M. N. Wilson, *Superconducting Magnets,* Oxford: Clarendon, 1983.

77. P. Wanderer et al., Partial lifetime test of an SSC collider dipole, *IEEE Trans. Magn.,* **30**: 1738–1741, 1994.

78. T. Schneider and P. Turowski, Critical current degradation of a NbTi-multifilament conductor due to heat treatment, *IEEE Trans. Magn.,* **30**: 2391–2394, 1994.

79. A. Devred et al., Investigation of heater-induced quenches in a full-length SSC R&D dipole, in T. Sekiguchi and S. Shimamoto (eds.), *Proc. 11th Int. Conf. Magn. Technol.,* London: Elsevier, 1990, pp. 91–95.

80. A. Devred et al., Quench characteristics of full-length SSC R&D dipole magnets, *Adv. Cryog. Eng.,* **35** (A): 599–608, 1990.

81. L. Coull et al., LHC magnet quench protection system, *IEEE Trans. Magn.,* **30**: 1742–1745, 1994.

82. R. Stiening et al., A superconducting synchrotron power supply and quench protection scheme, *IEEE Trans. Magn.,* **MAG-15**: 670–672, 1979.

83. K. Koepke et al., Two cell doubler system test, *IEEE Trans. Magn.,* **MAG-17**: 713–715, 1981.

84. W. Burgett et al., Full-power test of a string of magnets comprising a half-cell of the superconducting super collider, *Part. Accel.,* **43**: 41–75, 1993.

85. F. Rodriguez-Mateos et al., Electrical performance of a string of magnets representing a half-cell of the LHC machine, *IEEE Trans. Magn.,* **32**: 2105–2108, 1996.

ARNAUD DEVRED
Atomic Energy Commission at Saclay